

Design of effective fins for fast PCM melting and solidification in shell-and-tube latent heat thermal energy storage through topology optimization

Alberto Pizzolato^{a,*}, Ashesh Sharma^b, Kurt Maute^b, Adriano Sciacovelli^c, Vittorio Verda^a

^a Department of Energy, Politecnico di Torino, Corso Duca degli Abruzzi 24, Turin, Italy

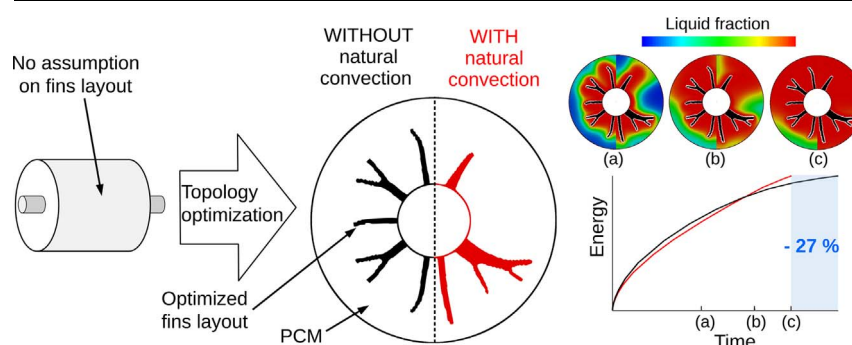
^b Department of Aerospace Engineering Sciences, University of Colorado at Boulder, Boulder, CO, USA

^c Birmingham Center for Energy Storage (BCES), School of Chemical Engineering, University of Birmingham, UK

HIGHLIGHTS

- High conducting fins are designed using topology optimization and computational fluid dynamics.
- Neglecting fluid flow in the analysis leads to suboptimal configurations.
- Melting and solidification are enhanced through natural convection with specific design features.
- Melting and solidification demand for fundamentally different fin layouts.

GRAPHICAL ABSTRACT



ARTICLE INFO

Keywords:

Heat transfer enhancement
Phase change materials (PCM)
Solidification & melting
Thermal energy storage
Topology optimization

ABSTRACT

This paper presents a unique solution to the problem of heat transfer intensification in shell-and-tube latent heat thermal energy storage units by means of high conducting fins. We developed a design approach using topology optimization and multi-phase computational fluid dynamics. No assumption is made about the fins layout, which freely evolves along the optimization process resulting in more efficient non-trivial geometries. At each optimization iteration, the fluid-dynamic response in the phase change material is computed by solving the transient Navier-Stokes equations augmented with a phase-change porosity term. Coupling large design freedom to detailed physics modeling allowed studying the effect of convective transport on both design and performance of latent heat thermal storage units. Results indicate that accounting for fluid flow in design optimization studies is crucial for performance. It is shown that melting and solidification can be enhanced remarkably through natural convection by using well engineered fins with specific design features, that could hardly be revealed with alternative design routes. These features make designs optimized for melting fundamentally different from those optimized for solidification.

1. Introduction

High energy density and nearly constant operating temperatures make Phase Change Material (PCM) an attractive option for Thermal Energy Storage (TES). High energy density results in compact units that

yields a reduction of investment cost for the tank envelope [1] and allows dealing with available space limitations [2]. A nearly constant operating temperature of the Heat Transfer Fluid (HTF) improves efficiency and extends operation time of downstream systems [3]. However, the low thermal conductivity of PCM limits the amount of energy

* Corresponding author.

E-mail address: alberto.pizzolato@polito.it (A. Pizzolato).

Nomenclature

A_{mushy}	mushy constant
c_p	specific heat
C_k	diffusivity ratio
d	truncation error estimate
E	energy
e_i	unit vector
F	momentum source term
f	liquid fraction
\mathbf{g}	gravity vector
L	reference length
\mathbf{n}	normal vector
p	pressure
q_α	Brinkmann interpolation constant
q_f	conductance interpolation constant
\mathbf{R}	vector of residuals
r	radius
r_f	filter radius
\mathbf{s}	vector of design variables
\tilde{s}	filtered design variable
\bar{s}	projected design variable
T	temperature
t	time
U	reference velocity
\mathbf{u}	vector of degrees of freedom
V	volume
\mathbf{v}	velocity
	objective function

Greek symbols

α_b	Brinkmann constant
α_t	thermal diffusivity
β	projection steepness parameter
Γ	boundary

δ_t	time integration tolerance
η	projection threshold
λ	vector of Lagrange multipliers
ξ_{log}	logistic constant
ρ_0	reference density
Φ	volume fraction
Ψ	energy fraction
Ω	domain
ω	filter weight

Dimensionless groups

Da	Darcy number
Pr	Prandtl number
Ra	Rayleigh number
Ste	Stefan number

Superscripts

$*$	dimensionless
fc	fully charged

Subscripts

b	Brinkmann
D	design
d	Dirichlet
$extr$	extrapolated
f	final
L	latent
m	melting
max	maximum
min	Minimum
N	Neumann
P	PCM
p	predicted

that can be stored and retrieved in a given amount of time. This reduces the spectrum of real-life applications. Most applications require for quick response to fast transients, which originates from generation [4] or demand peaks [5,6]. Using highly conductive fins is a possible way to enhance performance of the storage unit. This option has the advantage of low construction cost and ease of fabrication and maintenance [7] compared to other heat transfer enhancement approaches [7,8].

Over the last two decades the development of finned Latent Heat Thermal Energy Storage (LHTES) devices (e.g. shell-and-tube configuration), the study of the mutual link between design and performance (e.g. effect of geometry parameters) and ultimately the optimization of LHTES have been dominated by two modeling approaches: computational fluid-dynamics (CFD) and lumped parameters models (LPM). Through the use of CFD and LPM researchers have made significant progress in the design of LHTES units [9–11]. However both CFD and LPM have been used to perform only heuristic or parametric optimization studies [12,13], where the goal is usually to assess how the performance of a preconceived configuration is affected by design parameters (e.g. fins diameter, fins thickness, pipe diameter, etc.). Examples of such approach include the study of the effect of: fin length on the charge/discharge process [14], fins orientation [15,16], and fin spacing [12]. These valuable contributions, and the many more summarized in [11,17], show however that the initial configuration and the parameters selected are crucial. The analyst, on the basis of her/his insight into the problem, a priori selects the initial configuration (e.g. circular fins) and the parameters (e.g. fins diameter, thickness and orientation) to vary during the optimization procedure. Such an approach

clearly limits the amount of possible layouts explored. As a result, multiple heuristically improved shell-and-tube LHTES units with fins can be found in literature [9,11,18].

In a recent work [19], we have demonstrated the use of topology optimization for the design of high conducting fins in LHTES. From a design point of view, this approach is free of heuristics. The layout of finning material within the shell is not assumed a priori; rather it freely evolves resulting in more efficient non-trivial designs. We have focused on solidification because the average heat transfer rate is significantly lower than in melting [20] and neglected fluid flow considering solidification as dominated by heat conduction [18].

Using physics reduction for design optimization studies is questionable: whether convective effects matter strongly depends on the design. Clear evidence was presented by Vogel [21] who showed both numerically and experimentally that heat transfer enhancement due to natural convection increases with greater widths and smaller heights of storage material enclosures. Darzi et al. [22] compared the use of a non-finned elliptical HTF pipe to the use of a circular pipe with highly conductive fins for both melting and solidification enhancement. It was found that fins are highly effective for solidification but yield negligible contributions for melting. The use of elliptical pipes resulted in the opposite effect: melting is enhanced but solidification is not. Beck et al. [23] studied the performance of helical, transversal and longitudinal fins to enhance both melting and solidification. For melting enhancement, they recommended longitudinal fins since they guarantee unrestricted natural convection. On the other hand, no design was found to particularly favor solidification.

The above studies suggest that a priori assumption of negligible convective transport restricts the design space and may lead to a sub-optimal layout. Most of the reviewed literature focuses either on melting or on solidification, depending on the target application. For instance, storage units for off-peak refrigeration systems [24,25] can take considerable time for freezing but melting is required over a short period during the day. On the other hand, storage units in district heating systems [5] have to be designed to maximize the solidification rate: they are charged during the night and discharged during the day. Few guidelines [22,23] were reported on the essential design differences between heat transfer structures enhancing melting and solidification.

Considering the above mentioned shortcomings, the objectives of this paper are: (i) to demonstrate the use of topology optimization for designing LHTES units for enhanced melting and solidification; (ii) to analyze how the optimized designs are affected by fluid flow and understand how they exploit convective transport; (iii) to study what makes a structure optimized for melting different from one optimized for solidification.

Topology optimization originated in the structural community with the seminal work of Bendsoe [26] and Zhou and Rozvany [27] who proposed the Solid Isotropic Material with Penalization (SIMP) method or power-law approach. They introduced a fictitious porous material with normalized density ρ to define a continuous transition between two or more materials. The normalized density is treated as the design variable and is used to interpolate the material properties. The interpolation is formulated in such a way to make intermediate densities unattractive such that the optimization process converges to designs with well-distinct material domains. This approach gained maturity in the structural community and quickly extended to many other fields [28], e.g. fluid-dynamics [29–31] and heat transfer [32–36]. A schematic of topology optimization for the design of shell-and-tube LHTES is given in Fig. 1. A horizontal tube filled with a HTF stream is surrounded by both a PCM and a Highly Conductive Material (HCM), which occupy the external container. The design optimization problem is initialized as a homogeneous density distribution, corresponding to an amorphous homogeneous material with intermediate properties. Then, the optimization framework distributes HCM to obtain an optimized heat transfer structure.

The remainder of this paper is organized as follows. Section 2 presents the formulation of the design optimization problem for heat transfer enhancement in LHTES. In Section 3, the governing equations along with the temporal and spatial discretization schemes are given. Section 4 presents the computational aspects of topology optimization which are relevant to this problem while Section 5 focuses on the numerical implementation of the proposed optimization approach. Section 6 reports verification and validation studies of the used modeling framework and Section 7 presents the numerical studies and discusses the results obtained. Finally, Section 8 summarizes the main findings and identifies possible directions for future work.

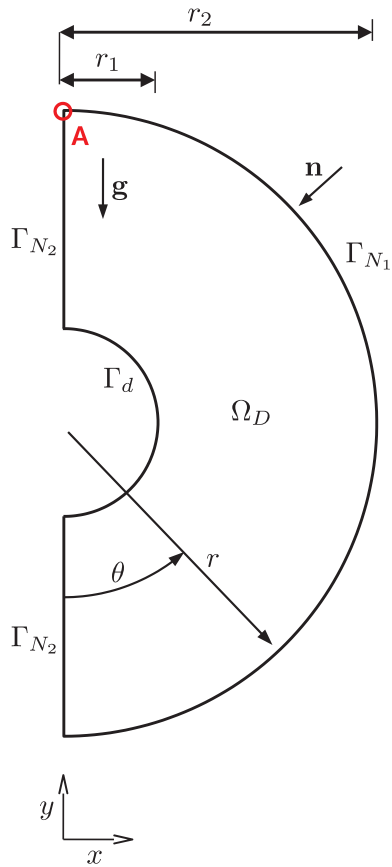
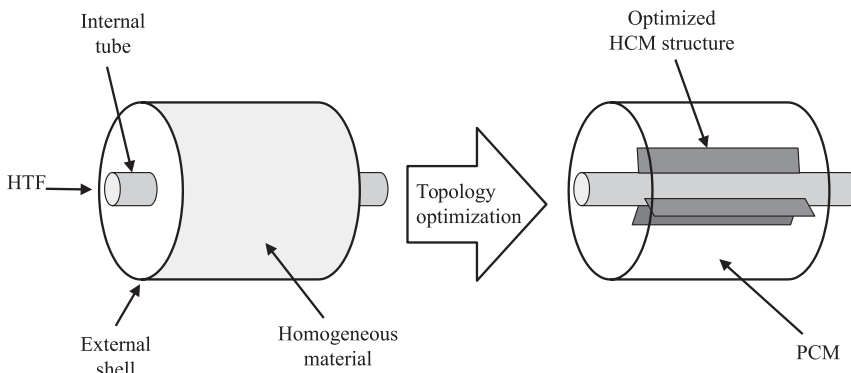


Fig. 2. Schematic of the design domain considered.

2. Design optimization of PCM storage units

In this paper, we seek to accelerate the discharge/charge process of a LHTES unit by optimizing the distribution of HCM embedded in PCM. Fig. 2 shows a schematic of the design domain Ω_D , which is filled with a fictitious composite material composed of PCM and HCM. Temperature T_d is prescribed at the internal boundary Γ_d to represent the contact with the pipe containing the HTF. A homogeneous Neumann boundary condition is prescribed on Γ_{N1} to describe an adiabatic boundary (external envelope) and on Γ_{N2} to account for symmetry. The direction of gravity is indicated in the schematic through the vector \mathbf{g} .

The design problem objective is the reduction of the dimensionless time t_f^* needed to charge/discharge the storage unit to a specified energy fraction Ψ of the fully charged tank. Hence, we formulate the optimization problem as:

Fig. 1. Representative visualization of optimization of finning material distribution in LHTES. The Heat Transfer Fluid flows in the tube while the PCM occupies the external envelope.

$$\begin{aligned}
& \underset{\mathbf{s}}{\text{minimize}} \quad z(\mathbf{u}(\mathbf{s}), \mathbf{s}) = t_f^* \\
& \text{subject to} \quad E - \Psi E^{fc} = 0 \quad \text{at} \quad t^* = t_f^* \\
& \quad V_{HCM} - \Phi \int_{\Omega_D} dV \leq 0 \\
& \quad \mathbf{s} \in \mathbf{S} = \{\mathbf{R}^{N_s} | s_{min} < s_i < s_{max}, i = 1, \dots, N_s\}
\end{aligned} \quad (1)$$

where z is the objective function, \mathbf{u} is the vector of degrees of freedom and \mathbf{s} is the vector of design variables, which represents the local volume fraction of the PCM and HCM phases. The equality constraint ensures that the energy level in the tank E reaches a specific fraction Ψ of the fully charged condition E^{fc} at time t_f^* . The inequality constraint, referred to as the volume constraint, prescribes that the ratio of volume of the HCM to the total volume should be lower than the volume fraction Φ . It aims at preventing the trivial solution of having the entire design domain filled with HCM. Lastly, the box constraint sets a lower bound $s_{min} = 0$ and an upper bound $s_{max} = 1$ to each local volume fraction s_i in the N_s -dimensional design space.

We adopt the nested analysis and design approach, which treats the state variables \mathbf{u} as dependent variables of \mathbf{s} . Therefore the thermal and fluid-dynamic responses need to be evaluated at each iteration of the optimization process.

3. Physical model

In this section, we provide a description of the physical problem solved and the corresponding governing equations. We then discuss approaches adopted for discretizing the governing equations in both space and time.

3.1. Governing equations

We formulate the governing equations in non-dimensional form using the following non-dimensional variables:

$$x_i^* = x_i/L \quad (2)$$

$$t^* = (t\alpha_t^{(p)})/L^2 \quad (3)$$

$$u_i^* = u_i/U \quad (4)$$

$$p^* = p/(\rho_0 U^2) \quad (5)$$

$$T^* = \frac{T - T_{min}}{T_{max} - T_{min}} \quad (6)$$

where x_i is the spatial dimension, t is the time, u_i is the velocity, p is the pressure and T is the temperature. All dimensionless quantities are marked with an asterisk. The reference constants adopted are: the reference length $L = r_2$, the minimum temperature T_{min} and maximum temperature T_{max} registered during the entire process, the PCM thermal diffusivity $\alpha_t^{(p)}$, the PCM reference density ρ_0 and the PCM diffusion velocity U calculated as:

$$U = \frac{\alpha_t^{(p)}}{L} \quad (7)$$

We model the phase change phenomenon through an enthalpy-porosity approach which does not require an explicit tracking of the melting front. Under the assumption of constant fluid properties, incompressible flow and negligible viscous dissipation, the dimensionless version of the Navier-Stokes and energy equations can be casted in the following form:

$$\frac{\partial v_i^*}{\partial x_j^*} = 0 \quad (8)$$

$$\frac{\partial v_i^*}{\partial t^*} + u_j^* \frac{\partial v_i^*}{\partial x_j^*} = -\frac{\partial p_i^*}{\partial x_i^*} + Pr \frac{\partial}{\partial x_j^*} \left(\frac{\partial u_i^*}{\partial x_j^*} + \frac{\partial u_j^*}{\partial x_i^*} \right) - RaPr e_i^g T^* + F_{bi}^*(s) + F_L^* \quad (9)$$

$$\frac{\partial T^*}{\partial t^*} + v_j^* \left(1 + \mathcal{L}^*(s) \frac{\partial f}{\partial T^*} \right) \frac{\partial T^*}{\partial x_j^*} = \frac{\partial}{\partial x_j^*} \left(K_{ij}(s) \frac{\partial T^*}{\partial x_i^*} \right) + q_L^* \quad (10)$$

where e_i^g is the unit vector in the direction of gravity, Pr is the Prandtl number, Ra is the Rayleigh number, $\mathcal{L}^*(s)$ is the design-dependent dimensionless latent heat, $K_{ij}(s)$ is the design-dependent dimensionless thermal diffusivity, $F_{bi}^*(s)$ is a design-dependent momentum source term, F_L^* is a phase change-related momentum term and q_L^* is a phase change-related energy source term. Eq. (8) commonly referred to as continuity equation, is a kinematic constraint prescribing a divergence-free flow. Eq. (9) enforces the conservation of momentum along the ' i ' direction. The dimensionless momentum source term F_L^* ensures the velocity field is zero in the solid PCM region. It is written as a modified version of the Kozeny-Carman equation [37]:

$$F_L^* = \frac{A_{mushy} (1-f)^2}{\rho_0 U/L f^3 + \zeta} u_i^* \quad (11)$$

where $\zeta = 10^{-3}$ is a small constant to avoid division by zero, $A_{mushy} = 10^8 \text{ kg}/(\text{m}^3 \text{ s})$ [38] is the mushy constant describing how steeply the velocity is driven to zero when the material solidifies. The mushy zone is defined as the area enclosed between the liquidus and the solidus line, containing PCM that is not fully solid nor fully liquid. The variable f is a temperature-dependent function that quantifies the relative amount of PCM in liquid phase. To allow for differentiability, the following logistic distribution function is used rather than a piecewise formulation:

$$f(T^*) = \frac{1}{1 + \exp(-\xi_{log}(T^* - T_m^*))} \quad (12)$$

where T_m^* is the mean melting temperature and $\xi_{log} = 15$ is a constant that controls the steepness of the logistic curve and is dependent on the temperature range of the mushy zone. The design-dependent momentum source term $F_{bi}^*(s)$ drives velocities to zero in the HCM portion of the design domain. It is written as a Brinkmann friction force as suggested in [39,29]:

$$F_{bi}^*(s) = -\alpha_b^*(s) u_i^* \quad (13)$$

where the property α_b^* physically corresponds to:

$$\alpha_b^* = \frac{Pr}{Da} \quad (14)$$

where Da is the Darcy number. Eq. (10) describes the convection and diffusion of energy in the form of both sensible and latent heat. The design dependent energy source term q_L^* accounts for the latent portion of the energy accumulation term and is written as [40]:

$$q_L^* = -\mathcal{L}^*(s) \frac{\partial f}{\partial t^*} \quad (15)$$

The set of design dependent properties, i.e. $\mathcal{L}^*(s)$, $\alpha_b^*(s)$ and $K(s)$ are continuously interpolated in such a way to recover consistent material properties, i.e.:

$$\{\mathcal{L}^*, \alpha_b^*, K_{ij}\} = \begin{cases} \{0, \infty, C_k^{-1} \delta_{ij}\} & \text{represents HCM} \\ \{Ste^{-1}, 0, \delta_{ij}\} & \text{represents PCM} \end{cases} \quad (16)$$

where Ste is the Stefan number, $C_k = \alpha_t^{(p)}/\alpha_t^{(H)}$ is the diffusivity ratio between PCM and HCM and δ_{ij} is the Kronecker delta. Note that in the HCM portion, which is ruled by pure diffusion, the velocity is driven to zero by the Brinkmann momentum sink of Eq. (9) making the second term of the left-hand side in Eq. (10) disappear. Further details on the interpolation strategy are left for Section 4.1.

We prescribe an adiabatic boundary on the external shell Γ_{N_1} and a symmetry boundary condition on Γ_{N_2} such that:

$$-\frac{\partial T^*}{\partial x_j^*} \mathbf{n} = \mathbf{0} \quad \text{on} \quad \Gamma_{N_1} \cup \Gamma_{N_2}, \quad \forall t \quad (17)$$

Temperature is fixed at the internal boundary Γ_d to represent the contact with the tube containing the HTF. Mathematically:

$$T^* = T_d^* \quad \text{on } \Gamma_d, \quad \forall t \quad (18)$$

where T_d^* is the HTF pipe dimensionless temperature, that takes different values for charge and discharge. The interaction with the external shell boundary and the pipe boundaries is modeled using a no-slip condition. Due to symmetry, only non-penetration is prescribed on the boundary running along the y-axis. Mathematically:

$$u_i^* = 0 \quad \text{on } \Gamma_d \cup \Gamma_{N_1}, \quad \forall t^* \quad (19)$$

$$u_i^* \cdot \mathbf{n} = 0 \quad \text{on } \Gamma_{N_2}, \quad \forall t^* \quad (20)$$

To obtain a well-posed incompressible Navier-Stokes problem, the pressure $p^* = 0$ is specified at point A (Fig. 2). This choice does not modify the thermal and fluid-dynamic responses. The initial conditions are:

$$\begin{aligned} T^* &= T_I^* \quad \text{in } \Omega_D, \quad \text{at } t^* = 0 \\ u_i^* &= 0 \quad \text{in } \Omega_D, \quad \text{at } t = 0 \\ p^* &= 0 \quad \text{in } \Omega_D, \quad \text{at } t = 0 \end{aligned} \quad (21)$$

where T_I^* is an initial dimensionless temperature field.

3.2. Spatial discretization

The weak form of Eqs. (8)–(10) are obtained by multiplying the governing equations with a set of admissible test functions and integrating over the domain. In this paper, the weak form of the governing equations is discretized in space by four-node finite elements, where the velocity and pressure fields are approximated by bilinear, equal-order interpolations. We obtain the semi-discrete form:

$$\mathbf{R}(\mathbf{u}, \dot{\mathbf{u}}) = 0 \quad (22)$$

where \mathbf{R} is the vector of residuals, \mathbf{u} represents all the degrees of freedom (dimensionless velocities, pressures and temperatures) and $\dot{\mathbf{u}}$ is its time-derivative. The equal order interpolation for pressures and velocities fails to satisfy the Babuska-Brezzi condition [41] and results in an oscillating pressure field. Furthermore, the convective terms in the momentum and energy equation may cause spurious oscillations in the temperature field [42]. A similar behavior is observed if the thermal boundary layer is thinner than the mesh element size [43]. To prevent numerical instabilities, we augment the weak form of the governing equations with SUPG (Streamline Upwind Petrov-Galerkin), PSPG (Pressure Stabilized Petrov-Galerkin) and GGLS (Galerkin Gradient Least Squares) [41–43] stabilization terms which arise from the use of consistent Petrov-Galerkin weighting functions. Additional numerical instabilities were observed by Kreissl et al. [44] to arise from the SUPG stabilization of the Brinkman term. For this reason, we suppress the SUPG stabilization when $\alpha_b^* > 10^{-4}$ via a smoothed Heaviside-function with bandwidth $\delta\alpha_b^* = 10^{-4}$. For further details on this approach we refer to [44].

3.3. Temporal discretization and adaptive time-stepping

Eq. (22) is discretized in time using a first-order Backward Differentiation Formula (BDF). The time-derivative $\dot{\mathbf{u}}$ is written as:

$$\dot{\mathbf{u}}^{(n+1)} = \left(\frac{\partial \mathbf{u}}{\partial t^*} \right)^{(n+1)} = \frac{\mathbf{u}^{(n+1)} - \mathbf{u}^{(n)}}{(\Delta t^*)^{(n)}}, \quad n = 1, \dots, N_t \quad (23)$$

where n is the time step index, N_t total number of time steps and Δt^* the time-step size. To allow for control over the local truncation error introduced by (23), the time-step size is changed using an adaptive scheme. In this paper, we adopt the approach suggested in [45]:

$$(\Delta t^*)_{ad}^{(n+1)} = (\Delta t^*)^{(n)} \left(a \frac{\delta_t}{d^{(n+1)}} \right)^b \quad (24)$$

where $a = 2$ and $b = 1/2$ for first order-schemes. The parameter δ_t is a user-specified error tolerance and $d^{(n+1)}$ is a local estimate of the truncation error. In the present paper, we adopt the formulation presented in [29]:

$$d^{(n+1)} = \left(\frac{1}{N_d \max(\mathbf{u})^2} \sum_{i=1}^{N_d} (u_i^{(n+1)} - u_{i_p}^{(n+1)})^2 \right)^{1/2} \quad (25)$$

where N_d is the number of degrees of freedom, $u_i^{(n+1)}$ is the solution computed with (23) and $u_{i_p}^{(n+1)}$ is the degree of freedom computed with the following extrapolation:

$$\mathbf{u}_p^{(n+1)} = \mathbf{u}^{(n)} + \Delta t^{*(n)} \dot{\mathbf{u}}^{(n)} \quad (26)$$

To enforce the final time constraint of (1), at each time step we estimate the remaining time $(\Delta t^*)_{extr}^{(n+1)}$ based on a linear extrapolation of the energy history:

$$(\Delta t^*)_{extr}^{(n+1)} = (\Delta t^*)^{(n)} \frac{\Psi E^{fc} - E^{(n+1)}}{E^{(n+1)} - E^{(n)}} \quad (27)$$

The fraction on the right-hand side is positive in both charge and discharge process due to the monotonicity of the energy history. The time-step $n + 1$ is then chosen as:

$$(\Delta t^*)^{(n+1)} = \min((\Delta t^*)_{ad}^{(n+1)}, (\Delta t^*)_{extr}^{(n+1)}) \quad (28)$$

The time solver is stopped when the final time constraint of (1) is satisfied within a specified relative tolerance ϵ_r . At time step $n = 0$ the discrete residual equations reduce to satisfy the initial conditions:

$$\mathbf{R}^{(0)} = \mathbf{u}^{(0)} - \mathbf{u} \quad (29)$$

For every time-step $n > 0$, we solve the nonlinear problem $\mathbf{R}^{(n)} = 0$ via Newton's method. The Jacobian $\mathbf{J}^{(n)}$ is obtained considering a static and a dynamic contribution as following:

$$\mathbf{J}^{(n)} = \frac{\partial \mathbf{R}}{\partial \mathbf{u}^{(n)}} \bigg|_{u^{(n)}} + \frac{\partial \mathbf{R}}{\partial \dot{\mathbf{u}}^{(n)}} \bigg|_{u^{(n)}} \frac{1}{\Delta t^{*(n)}} \quad (30)$$

where the second term has been obtained using the time integration scheme adopted.

4. Topology optimization

This section describes the most relevant aspects of topology optimization for the design problem considered, including the material interpolation strategy, the adjoint sensitivity analysis and the regularization and continuation schemes.

4.1. Material interpolation

To perform topology optimization, a fictitious porous material is introduced to continuously interpolate the design-dependent thermo-physical properties. The transition from HCM to PCM is defined by the vector of projected design variables $\bar{\mathbf{s}}$, through an explicit formulation. A discussion on how to obtain $\bar{\mathbf{s}}$ from the design variable field \mathbf{s} is presented in Section 4.3. In our convention, $\bar{s} = 1$ denotes fully fluid and $\bar{s} = 0$ fully solid. For intermediate values we define [34]:

$$K(\bar{s}) = \frac{\bar{s}(C_k(1 + q_f - 1) + 1)}{C_k(1 + q_f)\bar{s}} \quad (31)$$

$$\alpha^*(\bar{s}) = \alpha_{max}^* \frac{1 - \bar{s}}{1 + q_\alpha \bar{s}} \quad (32)$$

where q_f and q_α are convexity factors used to control the shape of the interpolation function at intermediate values of \bar{s} , and α_{max}^* is a large value whose choice is problem-dependent. The dimensionless latent heat is approximated with a simple linear interpolation as:

$$\mathcal{L}^*(\bar{s}) = Ste^{-1}\bar{s} \quad (33)$$

The values of the convexity parameters q_f and q_α as well as α_{max} should be chosen carefully. A mild penalization of the intermediate \bar{s} values would result in poor convergence to binary designs, i.e. with large regions occupied by intermediate \bar{s} material. Large penalization will increase nonlinearity and affect convergence of the optimization process. The parameters adopted in the present paper are the result of a set of preliminary numerical tests discussed in Section 4.4.

4.2. Adjoint sensitivity analysis

In the current study we adopt a gradient-based optimization method, which requires the derivatives of the objective and constraints with respect to the design variables. Topology optimization belongs to the particular class of optimization problems characterized by a large number of design variables and few constraints. For this class of optimization problems, the adjoint method is particularly convenient for the sensitivity analysis [46].

The design sensitivities with respect to the final time t_f^* are calculated by post-multiplying those obtained with respect to the final energy $E(t_f^*)$ as following:

$$\frac{dt_f^*}{ds} = \left(-\frac{dE}{dt^*} \bigg|_{t^*=t_f^*} \right)^{-1} \frac{dE(t_f^*)}{ds} \quad (34)$$

where the multiplication factor enclosed in brackets is obtained by linearizing the energy history of the unit around t_f^* . The discrete sensitivity field with respect to the final energy is calculated as: [47]:

$$\frac{dE}{ds} = \frac{\partial E}{\partial s} + \sum_{n=0}^{N_t} \lambda^{(n)T} \frac{\partial \mathbf{R}^{(n)}}{\partial s} \quad (35)$$

where N_t is the number of time steps of the forward analysis, $\lambda^{(n)}$ is the discrete adjoint field at time n , which is calculated by integrating the adjoint equation backward in time. For a first order BDF, we obtain the following recursive relation:

$$\left(\frac{\partial \mathbf{R}^{(n)}}{\partial \mathbf{u}^{(n)}} \right)^T \lambda^{(n)} = - \left(\frac{\partial E}{\partial \mathbf{u}} \right)^{(n)} + \frac{1}{\Delta t^{*(n+1)}} \left(\frac{\partial \mathbf{R}^{(n+1)}}{\partial \mathbf{u}^{*(n+1)}} \bigg|_{\mathbf{u}^{(n+1)}} \right)^T \lambda^{(n+1)} \quad (36)$$

for $n = N_t, \dots, 0$ and $\lambda^{N_t+1} = \mathbf{0}$. The adjoint method needs the solution of the physical system for computation of the adjoint field. For this reason, the solution of the physical system is stored for every time-step of the transient analysis. The adjoint solutions are calculated using the same time-steps used in the forward analysis. A similar procedure to Eqs. (35) and (36) is followed for the computation of the constraints sensitivities.

4.3. Regularization

Filtering is a popular regularization approach in topology optimization that ensures both mesh-independence and checkerboard-free results [48]. In the present paper, we use the normalized linear filter originally proposed by [49]. The filtered design variable field at node i is calculated as:

$$\tilde{s}_i = \left(\sum_{j=1}^{N_s} \omega_{ij} \right)^{-1} \sum_{j=1}^{N_s} \omega_{ij} s_j \quad (37)$$

where N_s is the number of nodes in the finite element mesh and ω_{ij} is the filter weight calculated as:

$$\omega_{ij} = \max(0, r_f - |\mathbf{x}_i - \mathbf{x}_j|) \quad (38)$$

where r_f is the prescribed filter radius.

This operator introduces some additional fuzziness in the material distribution, i.e. it *smooths* the design variable field gradients. To obtain crisp boundaries, density-based topology optimization approaches require projection schemes. Here we use the one proposed by Wang et al. [50]:

$$\bar{s}_i = \frac{\tanh(\beta\eta) + \tanh(\beta(\tilde{s}_i - \eta))}{\tanh(\beta\eta) + \tanh(\beta(1 - \eta))} \quad (39)$$

where \bar{s} is the projected design variable field, $\eta = 0.5$ represents the projection threshold while β is a parameter that controls the steepness of the projection. Note that in general this filtering and projection approach does not guarantee control on the minimum feature size [51]. We account for filtering and projection in the sensitivity analysis by applying the chain rule:

$$\frac{\partial(\cdot)}{\partial s_i} = \sum_{j=1}^{N_s} \sum_{k=1}^{N_s} \frac{\partial(\cdot)}{\partial \rho_{s_k}} \frac{\partial \rho_{s_k}}{\partial \tilde{s}_j} \frac{\partial \tilde{s}_j}{\partial s_i} \quad (40)$$

4.4. Continuation scheme

Similar to [52], we adopt a continuation scheme that helps in determining the final design and avoiding poor local minima. In particular, starting with a high q_α and/or low α_{max} favors the creation of highly conductive *permeable* branches, which do not disappear when q_α is lowered and/or α_{max} increased giving both a poor performing design and a highly oscillating optimization history. Raising q_f to too large values yields in most cases an elimination of small design details resulting in trivial heat transfer structures. As a part of the adopted continuation strategy, we raise the convexity parameter q_f (Eq. (31)) along with the β parameter of the projection in three steps (39) as follows:

$$\begin{aligned} \beta &\in \{1; 2; 4\} \\ q_f &\in \{1; 10; 10^2\} \end{aligned} \quad (41)$$

Each continuation step is considered complete when convergence of the optimization problem is reached. The remaining material interpolation parameters of (32) are held constant at $q_\alpha = 10$ and $\alpha_{max} = 10^7$.

5. Numerical implementation

A flow-chart of the topology optimization procedure is given in Fig. 3. After the initialization of the design variable field \mathbf{s} and the continuation parameters β and q_f , the physical problem is solved by a finite element analysis (Eq. (22)). We solve the non-linear systems of equations arising from the spatial and temporal discretization via a relaxed Newton method. The under-relaxation coefficient is set to 0.85 for the melting and solidification results presented in this paper and to 0.95 for the non-linear diffusion studies. These values have shown to be a good trade-off between reliable convergence and computational cost. The convergence criteria of the non-linear solver is set to a reduction of the relative residuals L_2 norm of 10^{-7} with respect to the initial. The linear systems at each Newton iteration of the forward analysis and at each time integration step of the sensitivity analysis are solved with the Multifrontal Massively Parallel sparse direct Solver (MUMPS) [53]. Time integration is performed through the adaptive time-stepping strategy given by Eq. (24). The initial time step is set to $\Delta t^* = 10^{-3}$ and the stopping tolerance $\epsilon_t = 10^{-3}$. The adaptive scheme allows controlling the local truncation error introduced by (23) but does not guarantee Newton stability. If the Newton convergence is not reached in the first 20 iterations, the time step is iteratively halved until convergence. This approach demonstrated to be robust enough to handle cases up to $Ra = 5 \cdot 10^5$.

The gradient of the objective and constraints are then computed in a sensitivity analysis step using the discrete adjoint method (Eq. (34) through Eq. (36)). The design sensitivities are used to update the design variable field using the Globally Convergent Method of Moving Asymptotes (GCMMA) [54]. The GCMMA solves a series of convex and separable subproblems obtained from the original problem. To ensure feasibility, some elastic design variables are introduced in the problem. In the present framework, the GCMMA subproblems are solved with a

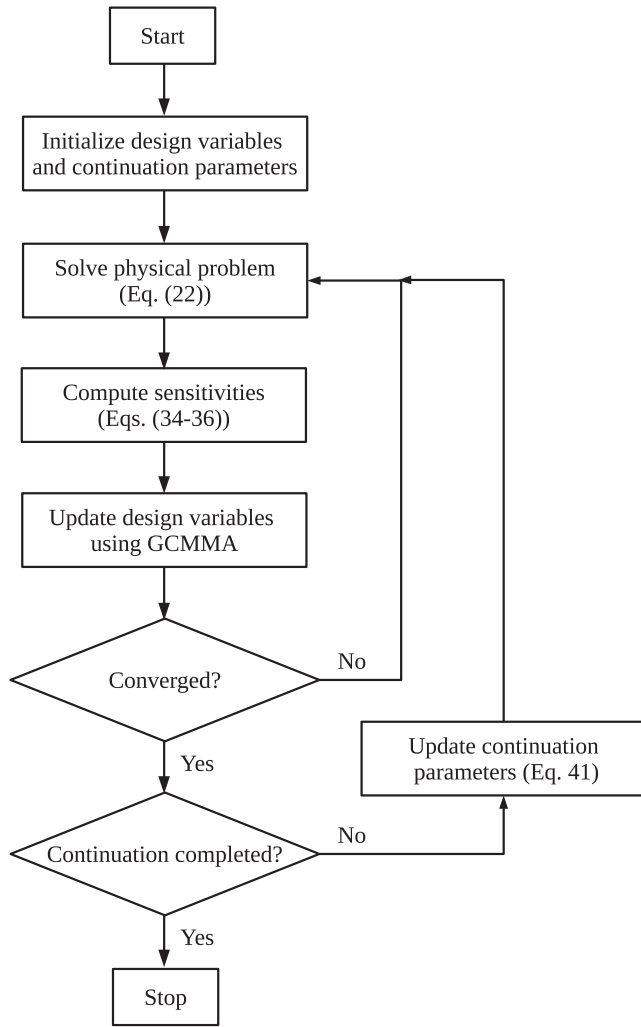


Fig. 3. Flowchart of the optimization procedure.

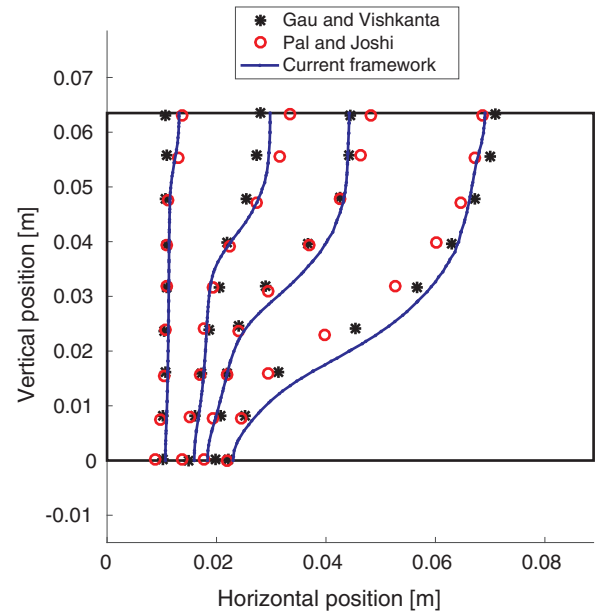
Table 1
GCMMA parameters utilized.

Step-size	0.03
Initial asymptote adaptivity	0.5
Lower asymptote adaptivity	0.7
Upper asymptote adaptivity	1.43
Constraint penalty	1000

primal–dual method. The relevant GCMMA parameters are provided in Table 1. Convergence of each continuation step detailed in (41) is considered satisfactory when the relative change in the objective is less than 10^{-3} for 5 consecutive iterations and all constraints are satisfied. The optimization procedure is considered complete when all the continuation steps (Eq. (41)) have been performed.

6. Verification and validation

The modeling framework in the current study has been validated using the experimental results reported by Gau and Vishkanta [55] for melting of gallium in a rectangular enclosure with vertical iso-thermal walls. The left and right wall are kept at $T = 311.15$ K and $T = 301.3$ K respectively. The initial temperature of the enclosure is set to $T = 301.3$ K. Fig. 4 shows a comparison of the melting front evolution between the numerical prediction of the presented framework, the experimental results of Gau and Vishkanta [55] and the numerical results

Fig. 4. Validation of the modeling framework against both experimental and numerical results in literature. Comparison of the $T = 302.93$ K iso-temperature lines atTable 2
Dimensionless numbers.

Diffusivity ratio	$C_k = 0.01$
Stefan number	$Ste = 0.05$
Dimensionless melting temperature	$T_m^* = 0.5$
Rayleigh number	$Ra = 10^5$
Prandtl number	$Pr = 30$

of Pal and Joshi [56]. A satisfactory agreement is observed indicating that our model is able to predict the phase change phenomenon with sufficient accuracy. To test the accuracy in shell-and-tube systems we included a verification study and a comparison with results obtained through COMSOL Multiphysics [57]. We focus on melting of a unit without fins. The design domain has dimensions $r_1 = 0.3$ and $r_2 = 1$. The dimensionless quantities are summarized in Table 2. We perform a mesh convergence study, comparing three different meshes with characteristic sizes $\Delta\theta = \{\pi/45; \pi/90; \pi/180\}$ to a reference mesh with $\Delta\theta = \pi/360$. The radial element size is calculated as $\Delta r = r\Delta\theta$. The charge time deviations computed with respect to the reference mesh are summarized in Table 3. A mesh with characteristic size $\Delta\theta = \pi/180$ with 12,851 quadrilateral elements was used to produce the results in Section 7. To verify independence of the results from the time-stepping strategy, we have run four analysis with different values of the integration tolerance δ_t . The charge times obtained with $\delta_t = \{0.04; 0.02; 0.01\}$ have been compared to that of a reference case with $\delta_t = 0.005$. Adopting an integration tolerance of $\delta_t = 0.01$ yields only a 0.21 % deviation from the reference case and was found sufficient to ensure time step independent results. A summary of this verification analysis is presented in Table 4. Fig. 5 shows the evolution of the iso-temperature line at $T^* = 0.5$ obtained with the current framework and with COMSOL Multiphysics [57]. The agreement indicates

Table 3
Mesh convergence verification. Deviation is calculated with respect to a reference case with $\Delta\theta = \pi/360$

Mesh characteristic size $\Delta\theta$ [–]	$\pi/45$	$\pi/90$	$\pi/180$
Deviation from reference [%]	5.24	1.01	0.48

Table 4

Time-stepping verification. Deviation is calculated with respect to a reference case with $\delta_t = 0.005$.

Integration tolerance δ_t [-]	0.04	0.02	0.01
Deviation from reference [%]	3.74	1.38	0.21

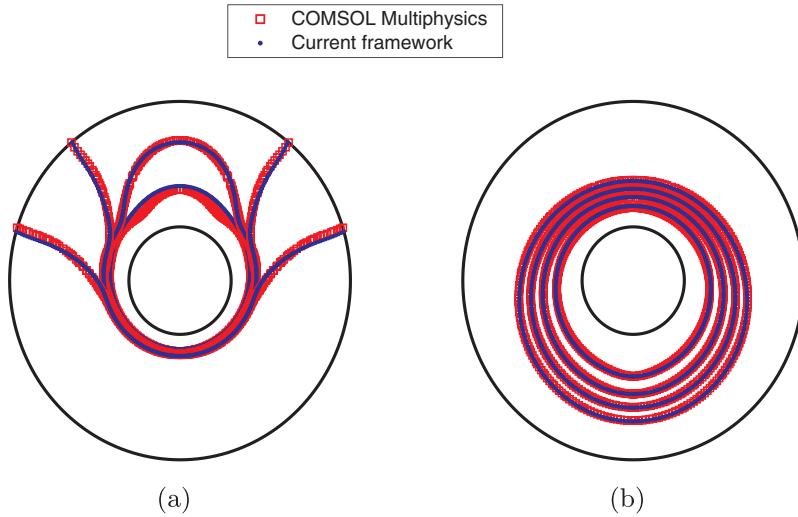


Fig. 5. Accuracy test of the current framework against COMSOL Multiphysics. Comparison of the $T^* = 0.5$ iso-temperature line at $t^* = \{1; 2; 3; 4\}$ for both melting (a) and solidification (b).

that our modeling framework is able to predict with sufficient accuracy the thermal and fluid-dynamic response in shell-and-tube LHTES units.

7. Results and discussion

This section presents the numerical studies and discusses the results obtained. First, we shed light on the topology optimization procedure focusing on the design optimization of a reference case with only diffusion. Then, we consider design optimization for a solidification and a melting case where we account for fluid flow. We study the most

7.1. Diffusion design

We first optimize the fin geometry for a case in which fluid flow is neglected. We consider a charge process, which is reproduced with a hot Dirichlet condition $T_d^* = 1$ and a cold initial temperature field $T_i^* = 0$. The charge is considered complete when the energy level in the tank reaches 95 % of the total capacity. We will refer to this case as the diffusive design hereafter. The objective history, normalized with respect to the initial value, along with the design at selected iterations is shown in Fig. 6. The initial design corresponds to a homogeneous

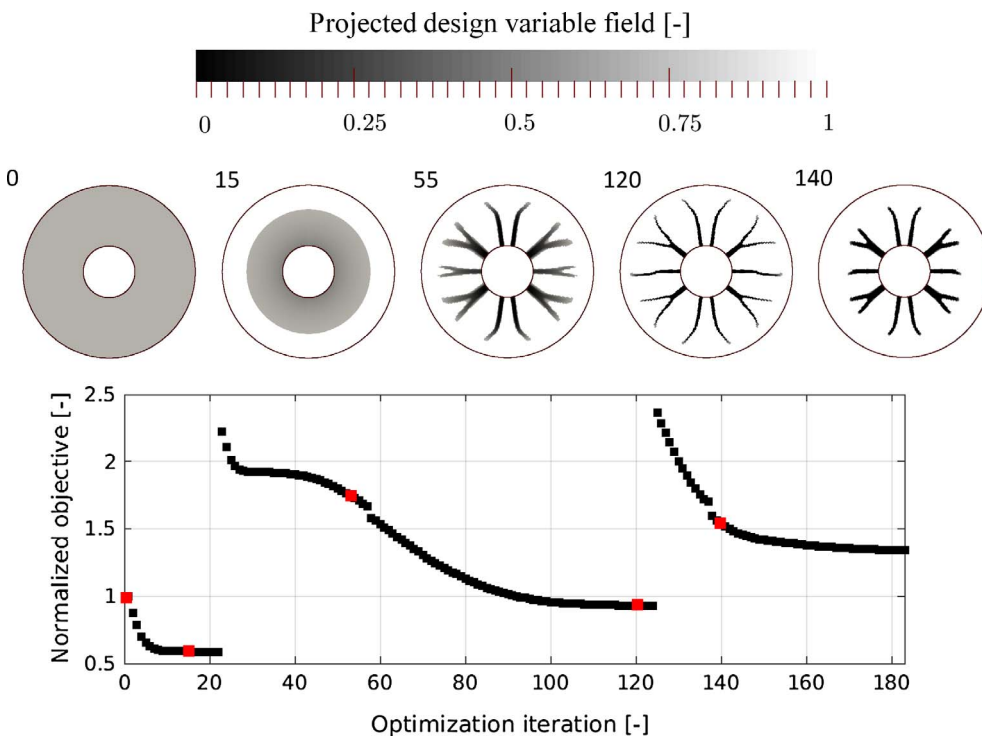


Fig. 6. Normalized objective history during the optimization of the diffusive design. The design evolution is shown at selected design iterations. Jumps in the objective corresponds to updates of the continuation scheme.

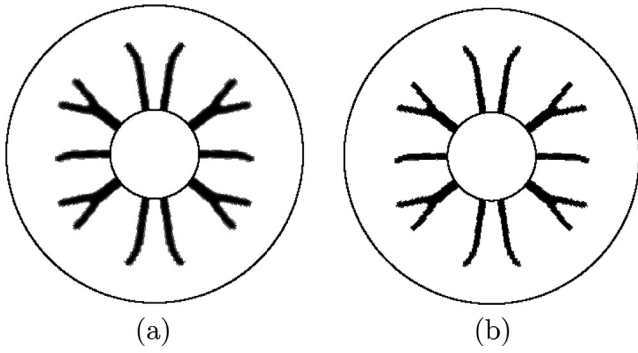


Fig. 7. (a): Final design obtained for the only diffusion case thresholded at $\bar{s} = 0.9$; (b): Final design obtained for the only diffusion case thresholded at $\bar{s} = 0.1$.

distribution $\bar{s} = 0.9$. In Fig. 6, the designs correspond to contour plots of the projected design variable field thresholded at $\bar{s} = 0.9$ to visualize the density field in the initial optimization iterations. The evolution of the objective shows three well-distinct stages, which correspond to the continuation scheme steps described in (41). In the first step, HCM concentrates in a region close to the internal tube and converges after 22 iterations. The second continuation step, which penalizes intermediate design variables more strongly, triggers ramification (iteration 55) and converges to a structure with extremely thin design features (iteration 120). With the third continuation step, those small design details characterized by intermediate design variables values disappear so that shorter and thicker fins are created. Note the three continuation steps are necessary to achieve good convergence to binary designs, i.e. where two distinct materials are recovered. Despite a lower objective function, the converged designs after the first and the second continuation step present large “gray” regions with intermediate densities. To quantify whether an optimized design has converged to a discrete solution we adopt a measure of non-discreteness similar to the one proposed by Sigmund [58]:

$$M_{nd} = \frac{\int_{\Omega_D} 4\bar{s}(1-\bar{s})dV}{\int_{\Omega_D} dV} \quad (42)$$

which intuitively represents the area fraction of the design domain in which the projected design variable has not fully converged to either 0 or 1. When there are no regions with intermediate design variable values, M_{nd} is 0 %. If $\bar{s} = 0.5$ everywhere, we would obtain $M_{nd} = 100$ %. The final optimized design obtained thresholding the projected design variable field at $\bar{s} = 0.5$ is shown in Fig. 8(a). The calculated measure of non-discreteness M_{nd} for this layout is 1.44 %. Fig. 7 shows how the optimized geometry depends on the threshold choice. The layout obtained thresholding the design variable field at $\bar{s} = 0.9$ (Fig. 7(a)) slightly differs from the one obtained with a threshold of $\bar{s} = 0.1$ (Fig. 7(b)) suggesting good convergence to a binary design. The optimized design is nearly symmetric with respect to the x-axis and shows quasi-periodicity along the angular direction with period $\Delta\theta = \pi/2$. The structure shows both longitudinal fins and Y-shaped (tree-like) fins around the HTF tube. The formers have been used extensively for heat transfer enhancement in LHTES, see for instance [59–61]. Tree-like fins with one or multiple bifurcations have been proposed and optimized in [62,20] and obtained as a topology optimization result in our previous work [19]. Interestingly, branched fins are alternated to non-branched radial HCM elements, similarly to the layout proposed by the Le Commissariat l’énergie atomique et aux énergies alternatives (CEA, France) [63]. Differently from [63], our optimized geometry does not reveal any circular high conducting insert.

7.2. Melting design

In this section we consider a melting process, i.e. the charge of a

LHTES unit. In this study, natural convection is considered. Referring to the boundary and initial conditions discussed in (18) and (21), to mimic melting we consider a hot Dirichlet condition $T_d^* = 1$ and a cold initial temperature field $T_i^* = 0$. Similarly to the diffusion design, the charge is considered complete when the energy level in the tank reaches 95 % of the total capacity. The optimized design obtained for melting is shown in Fig. 8(b). In this case, we obtain a measure of non-discreteness M_{nd} of 1.19 %. The melting design is profoundly different from the one obtained in Section 7.1: HCM concentrates in the bottom part of the storage unit to form a conductive-like structure that occupies the shell sector parameterized by $-\pi/3 < \theta < \pi/3$. To highlight the main layout differences between the two cases, Fig. 8(c) presents a superposition of the optimized designs for diffusion and melting. The design here is represented by the projected design variable field contour at $\bar{s} = 0.5$. We observe three main features. (i) The top portion of the unit shows only two short fins which are slightly offset from the radial direction. (ii) Two large and thick branches are visible at $\theta = -\pi/3$ and $\theta = \pi/3$ with second-order bifurcations. They also extend ~ 37.8 % more in the radial direction than the branches obtained in the diffusive case. (iii) Two thin branches elongates towards the bottom of the shell. These elements are ~ 19.6 % longer than the diffusive fins obtained at the same angular position. The radial position of the two thick branches described in (ii) resembles the results obtained in [64]. The authors observed that this particular configuration enhances heat transfer through convective transport. However, differently from our configuration, their design does not show any fin in the upper part of the unit and has a unique longitudinal fin elongating towards the bottom. The normalized energy histories of the two designs during a melting test are compared in Fig. 9. Here, both designs are analyzed considering the same physical model detailed previously, which considers the charge of the unit including fluid flow. Initially, the melting design shows a slower charge rate than the diffusion design. This is due to the fact that diffusion is the dominant heat transfer mechanism during the initial phase of the transient process. However, the heat transfer rate of the diffusion design slows down whereas the melting design maintains a fairly constant charge rate by exploiting the onset of natural convection. If the desired degree of charge of the storage units Ψ_c is above the limit value of 80.2 %, the convective design is the better performing choice. This limit is specific to the particular design domain and material properties considered in this paper. For the nominal design case, i.e. $\Psi_c = 95$ %, we obtain that the diffusion geometry demands for 25.9 % more time than the melting design to complete the charge process. Note that the particular choice of Ψ_c corresponds to an ideal utilization of the unit. Partial charge–discharge cycles are frequent in real systems. Fig. (10) shows the liquid fraction evolution at selected time instants of the melting test, corresponding to 20 %, 50 %, 80 % and 100 % of the total charge time of the melting design t_{jm}^* . At $t^* = 0.2 t_{jm}^*$ the liquid layer is too thin for natural convection to result in noticeable modifications of the melting front. During this initial stage of the process, the diffusion structure is more effective: thinner branches lead to more heat transfer area compared to the convective layout. As the fluid layer widens, natural convection starts modifying the shape of the melting front ($t^* = 0.5 t_{jm}^*$) and becomes dominant at $t^* = 0.8 t_{jm}^*$. The short fins of the melting design redirect the upward moving fluid layer in such a way that the liquid PCM quickly fills the upper part of the tank. The convective stream hardly reaches the region below the pipe, which is heated by long diffusive-like branches. The diffusion design can hardly get rid of the mushy region at the bottom of the tank. To better visualize the main heat transfer mechanisms, the magnitude of the average convective heat transfer rate \bar{q}_{vi} and of the conductive heat transfer rate \bar{q}_{ki} are depicted in Fig. 11. These quantities are calculated as:

$$\bar{q}_{vi} = \frac{\int_0^{t_{jm}^*} (v_i^*(T^* + fL^*))dt^*}{t_{jm}^*} \quad (43)$$

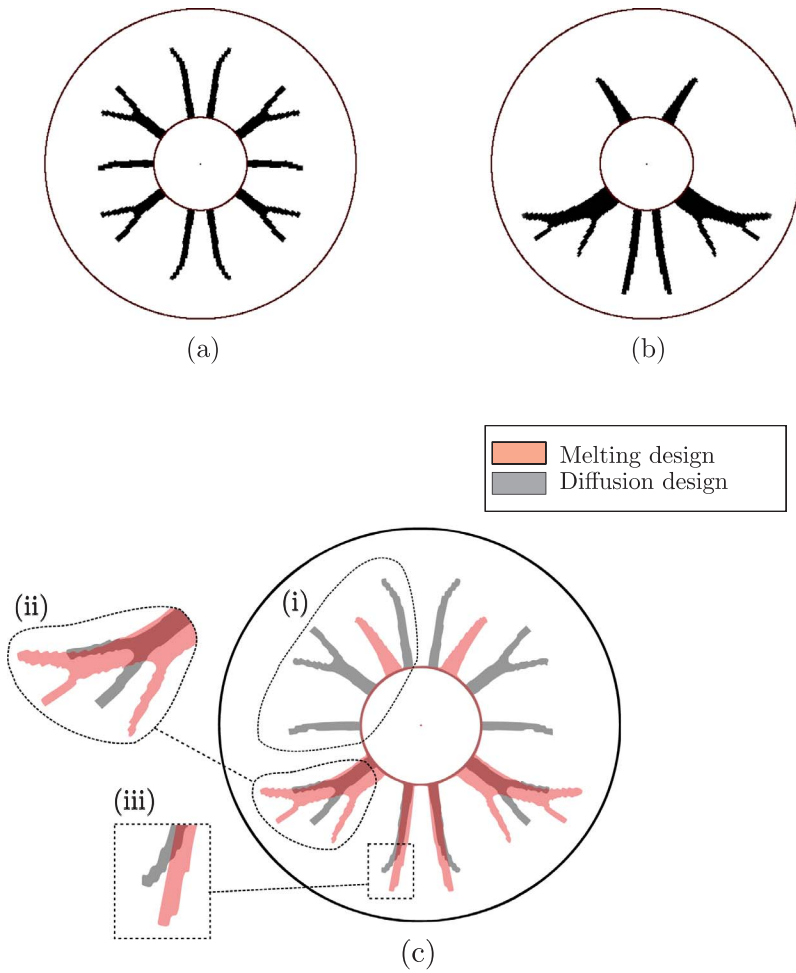


Fig. 8. (a): Final design obtained for the only diffusion case; (b): Final design obtained for the melting case; (c) Superposition of the two designs with zoom-in of the most relevant differences. The designs displayed have been obtained by thresholding the projected design variable field at $\bar{s} = 0.5$.

$$\bar{q}_{ki} = \frac{\int_0^{t_f^*} \left(-K_{ij} \frac{\partial T^*}{\partial x_j^*} \right) dt^*}{t_f^*} \quad (44)$$

The melting design largely utilizes the top fins and a portion of the pipe surface to enhance the convective heat transfer. This is confirmed by considering the conductive heat transfer plot which shows a large conductive contribution in the same region. A wide eddy maintains a high temperature gradient at the interface: hot fluid is rapidly

transported away leaving room for cold fluid coming from the outer part of the shell. This mechanism can be better observed in Fig. 12 where we show the average velocity magnitude alongside the streamlines. From a careful examination of the velocity plot, it is clear that the fins positioned above the pipe have the function of redirecting the flow towards the external shell. In the region below the pipe, convection is negligible and heat is transferred mainly by conduction. The ramification patterns of the diffusion design inhibit the formation of large convective eddies. The conductive heat transfer plot of the diffusion

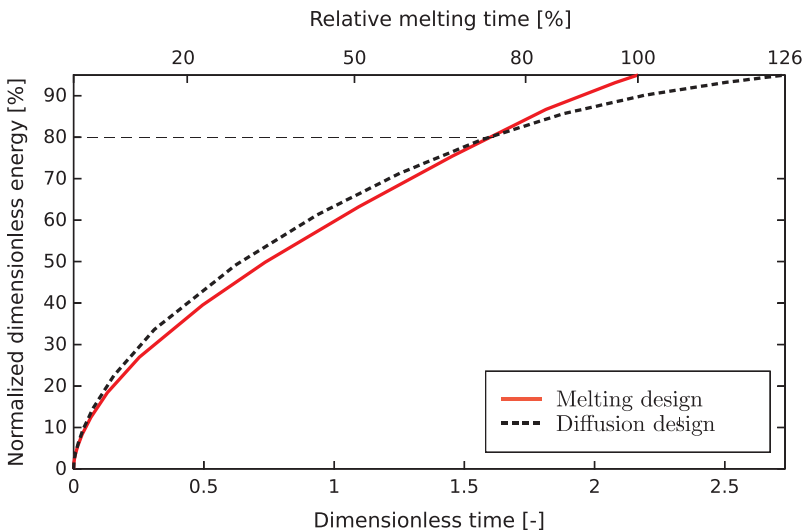


Fig. 9. Energy histories of the melting and diffusion designs during the melting test.

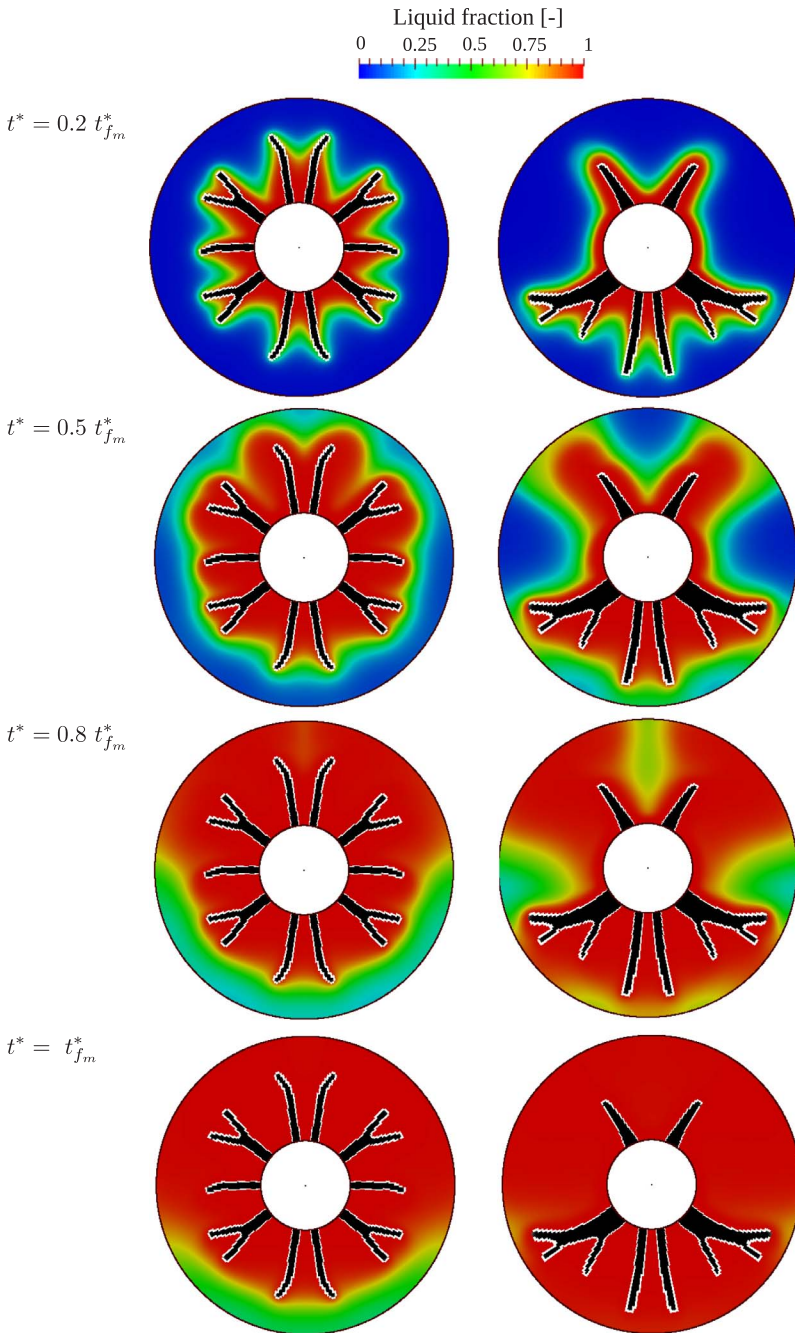


Fig. 10. Liquid fractions at selected time instants during melting. The left column shows the diffusion design while the right column shows the melting design.

design shows a high average heat transfer rate at the fin tips indicating that conduction takes place mainly in the radial direction.

This numerical study presents evidence that melting can be enhanced remarkably through convective transport if fins are designed with specific features, such as short baffles in the top portion of the unit and a big diffusive structure at the bottom.

7.3. Solidification design

Here we consider a solidification process corresponding to the discharge of the LHTES unit. Analogously to the previous section, we account for fluid flow. Solidification is introduced by considering a cold internal tube $T_d^* = 0$ (Eq. (18)) and a hot initial temperature field $T_i^* = 1$ (Eq. (21)). The discharge is considered complete when the energy level in the tank reaches 5 % of the total capacity. The optimized design obtained for solidification is shown in Fig. 13(b). The calculated

measure of non-discreteness M_{nd} for this layout is 1.37 %. The optimized diffusion design is shown again in Fig. 13(a) to facilitate comparisons. To highlight the main layout differences between the two cases, Fig. 13(c) shows a superposition of the optimized designs represented by the projected design variable field contoured at $\bar{s} = 0.5$. The solidification design closely resembles the one obtained considering only diffusion. However, accounting for natural convection in the analysis results in mainly four “convective” features. (i) Branches elongating towards the top of the shell are ~ 9.3 % longer than those of the diffusive design. (ii) Bifurcations of intermediate branches are not visible. (iii) Horizontal branches are ~ 43.7 % longer than those of the diffusive design. (iv) Branches elongating towards the bottom of the shell are ~ 3.2 % shorter than those of the diffusive design. The characteristics (i) and (iv) result in a higher concentration of HCM in the upper half the shell. This feature agrees with the intuition that a larger heat transfer area should be utilized in the regions where the

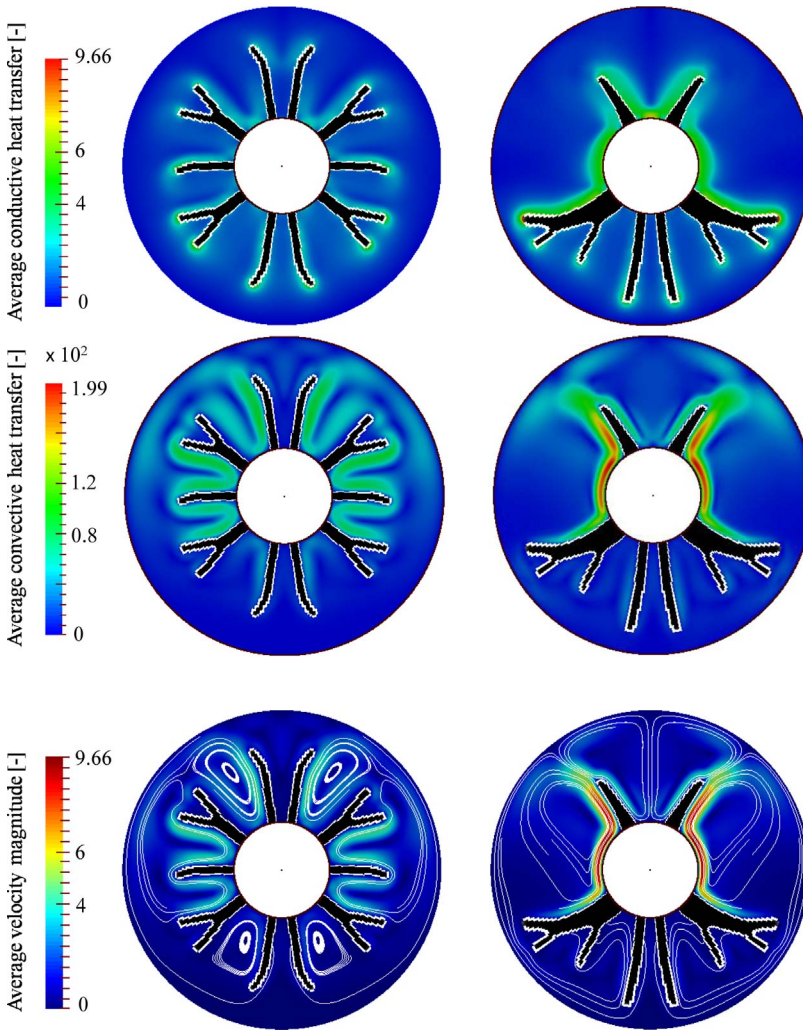


Fig. 11. Average heat conductive and convective heat transfer rate during melting. The left column shows the diffusion design while the right column shows the melting design.

Fig. 12. Average velocity magnitude with streamlines during melting. The left column shows the diffusion design while the right column shows the melting design.

solidification front lags behind. The obtained design is similar to the many longitudinal fins layouts utilized in literature, e.g. [59–61]. However, to our best knowledge no previous study in literature considers a varying fin length along the angular position in the shell, as described in (i), (iii), (iv). The normalized energy histories during solidification are shown in Fig. 14. The solidification design outperforms the diffusion design for any choice of the discharge fraction Ψ_d . The energy histories are very close to each other until $t^* \sim 0.45$, when they start to diverge. From this point onward, the temporal gap between the two curves increases linearly in time. Overall, the diffusion design demands for 11 % more time than the solidification design to discharge the unit. The liquid fraction evolution for the solidification test is shown in Fig. 15 at 20 %, 50 %, 80 % and 100 % of the discharge time of the solidification design t_{fs}^* . The solidification front shape has negligible differences for $t^* = 0.2 t_{fs}^*$ and $t^* = 0.5 t_{fs}^*$. Snapshots taken at $t^* = 0.8 t_{fs}^*$ and $t^* = t_{fs}^*$ show that the solidification design allows maintaining the solidus line nearly concentric with the internal tube thanks to the longer fins located above the pipe. In the meantime, the solidification front of the diffusion design starts drifting downward. This asymmetry with respect to the x-axis is responsible for the increased discharge time: the “left-over” mushy region at the top of the shell has to be cooled away for the discharge completion. Further insights can be gained by considering the average heat transfer rates in Fig. 16. The conductive portion in the diffusion design is concentrated at the fin tips similarly to what we observed for the same geometry in the melting test. On the other hand, the solidification design transports a non-negligible amount of conductive heat transfer along the fin sides. This

indicates that the solidification layout results in a more homogeneous heat transfer distribution and a better utilization of the fin material. In this case, the flow can penetrate close to the internal tube. On the other hand, the ramification patterns visible in the diffusion design inhibit this mechanism suppressing natural convection. From the examination of the streamlines shown in Fig. 17, we notice that the diffusion geometry confines the fluid outside the finned region. This creates a tall and thin eddy with a high downward velocity which contributes to the asymmetry of the solidus line discussed above. Conversely, the downward velocity in the solidification design is limited because of the small interstitial eddies and the longer horizontal fins. Fig. 17 also shows that the velocities involved in solidification are significantly lower than those involved in melting (Fig. 12). This limits the average heat transfer rate and results in longer time required for discharge compared to charge of the LHTES unit.

The results obtained in this sections indicate that bifurcations should be avoided to exploit convective transport in solidification and suggest to adopt a varying fin length along the angular direction. Furthermore, a comparison of this layout with the one obtained in Section 7.2 proves that geometries optimized for melting are in general different from those optimized for solidification.

7.4. Application to a small scale storage unit for district heating

In this section we test the performance of the optimized designs for a real world application: a small scale storage unit for district heating networks. Due to high compactness of the LHTES, the unit can be

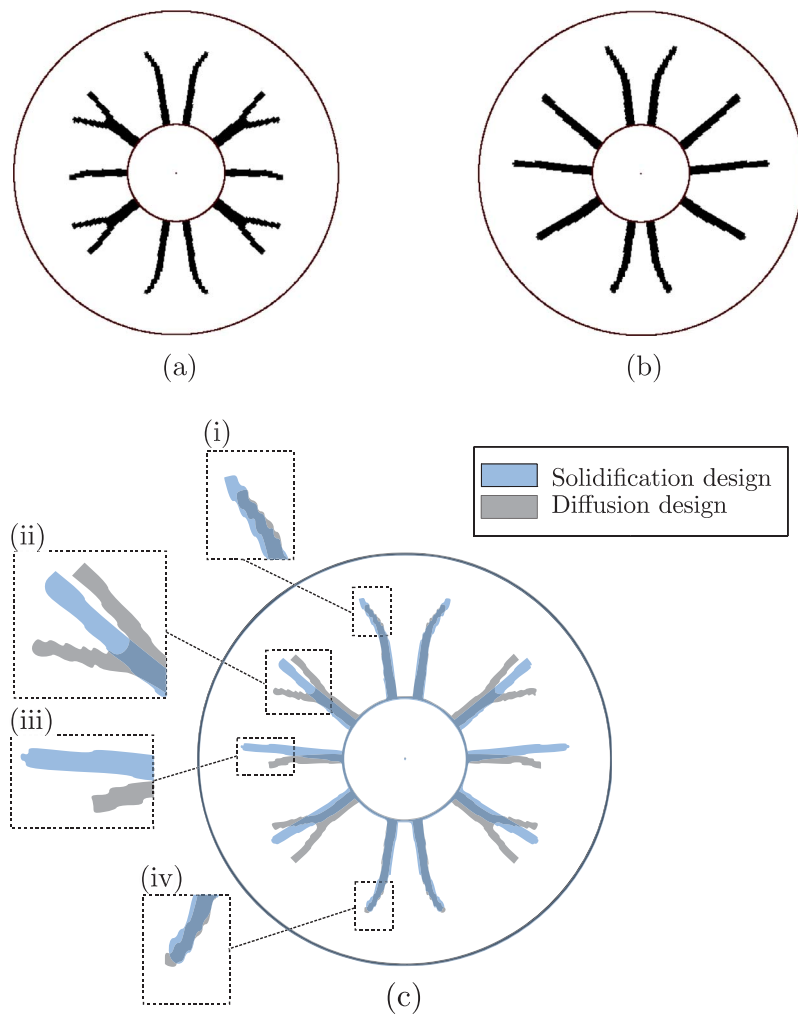


Fig. 13. (a): Final design obtained for the only diffusion case; (b): Final design obtained for the solidification case; (c) Superposition of the two designs with zoom-in of the most relevant differences. The designs displayed have been obtained by thresholding the projected design variable field at $\bar{s} = 0.5$.

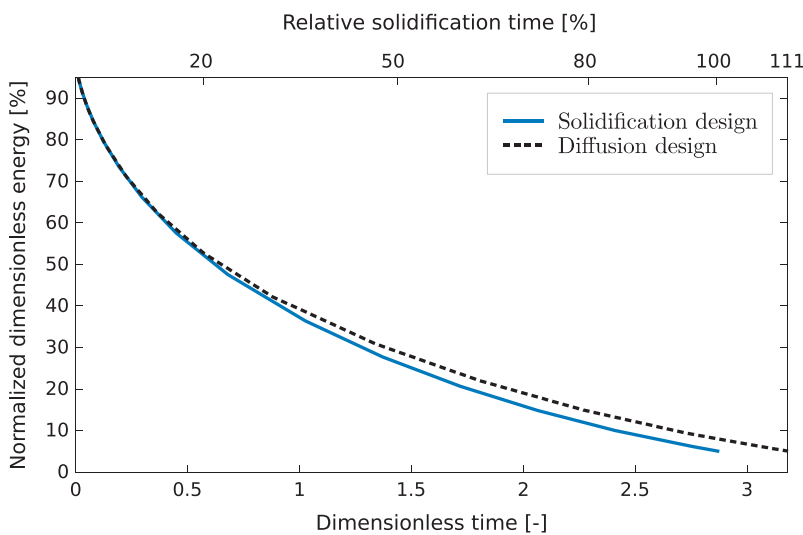


Fig. 14. Energy histories of the solidification and diffusion designs during the solidification test.

installed at each thermal user location in parallel to the building heat exchanger. We assume the building is heated by a low-temperature system. This allows placing the unit and the heat exchanger on the return line of the primary network, typically at 70 °C. We consider this value as boundary condition during charge. On the other hand, the HTF temperature during discharge is set to 20 °C, corresponding to the temperature of the secondary network at startup. The material

properties and the shell dimensions are the same used for a previous design study [65]. The radius of the HTF tube is here set to $r_1 = 0.0165$ m to keep consistency with the radius ratio adopted in this paper. Converting topology optimization results into manufacturable structures that can be used in real-world engineering applications is a non-trivial problem. The continuous nature of design variables in density-based topology optimization may result in unphysical optimization solutions,

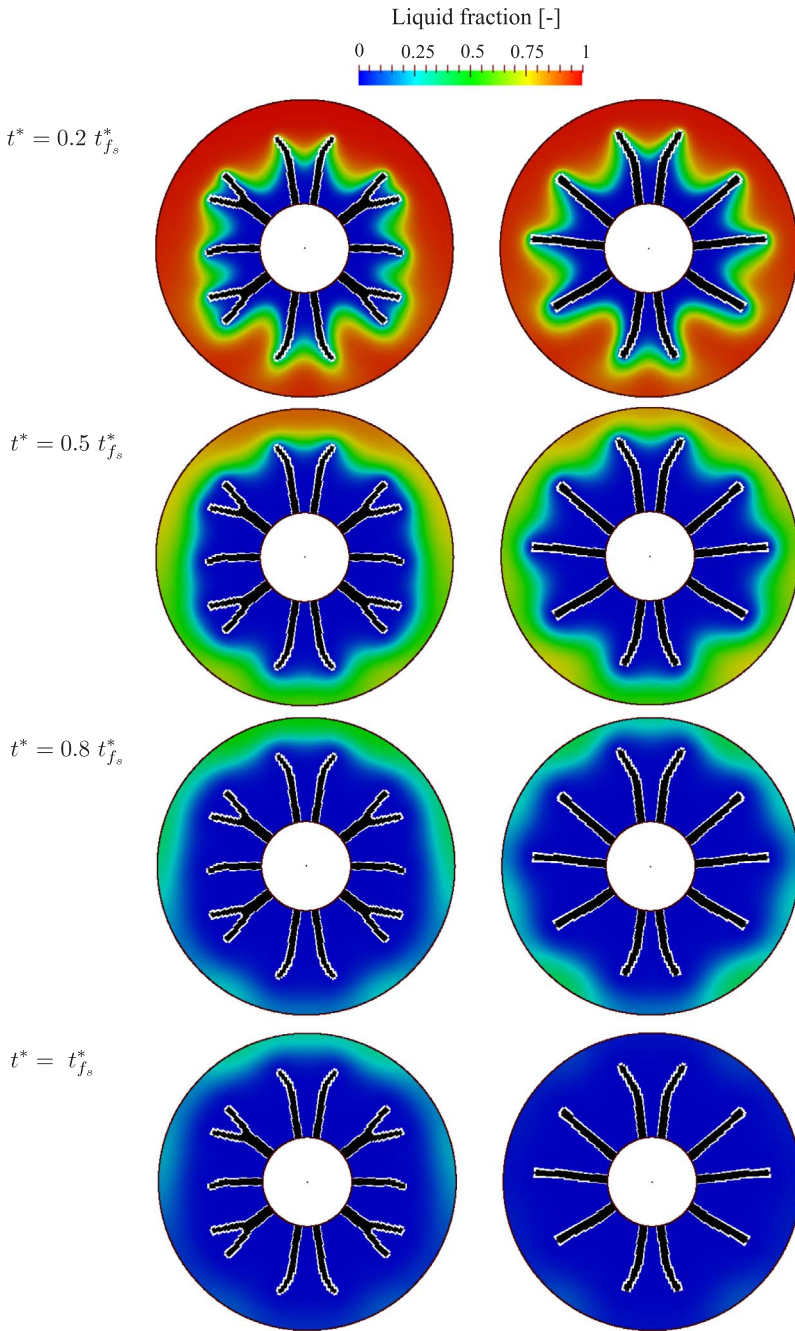


Fig. 15. Liquid fractions at selected time instants during solidification. The left column shows the diffusion design while the right column shows the solidification design.

with design domain regions occupied by intermediate s material. This makes necessary to post-process the optimized designs before manufacturing. A possible approach consists in *clipping* the density field at a certain threshold to obtain the final design. Care should be taken to ensure that the volume inequality constraint is still satisfied after this operation. The iso-surface of the clipped part can then be triangulated in a meshing software to obtain a STereoLithography (STL) file for direct manufacturing [66] or further derived into a Computer Aided-Design (CAD) model [67]. Through this strategy, we import CAD representations of the optimized designs into COMSOL Multiphysics [57] and analyze the performance using high-resolution body-fitted meshes. We consider both melting and solidification. For each case, three designs are compared: the optimized layout obtained with our topology optimization framework, a modified version with reduced complexity that allows for easier manufacturing and a classical design with longitudinal fins. Fig. 18 shows the procedure followed to reduce the

complexity of the topological layout. First, the optimized geometry (thresholded at $\bar{s} = 0.5$) is interpolated over a 300×300 grid (Fig. 18(a)). Then, a binary skeleton (Fig. 18(b)) is obtained through sequential thinning [68]. Branch junctions, bifurcations and extrema are then identified and linked with line segments to obtain a straight skeleton (Fig. 18(c)). Finally, a uniform fin thickness is calculated such that the HCM volume fraction is conserved equal to the original design. The obtained reduced layout is depicted in Fig. 18(d). The reduced layout obtained for the solidification case and the design with longitudinal fins are depicted in Fig. 19. The longitudinal design is composed of 10 fixed-length fins equally spaced along the angular direction. The fin length has been computed as average of those obtained in the reduced solidification layout. Note that the designs shown in Figs. 19(a) and 19(b) differ in terms of length and tilt angle of the fins.

Fig. 20 shows the performance of the analyzed geometries over a full charge and discharge. When using the topology optimized design,

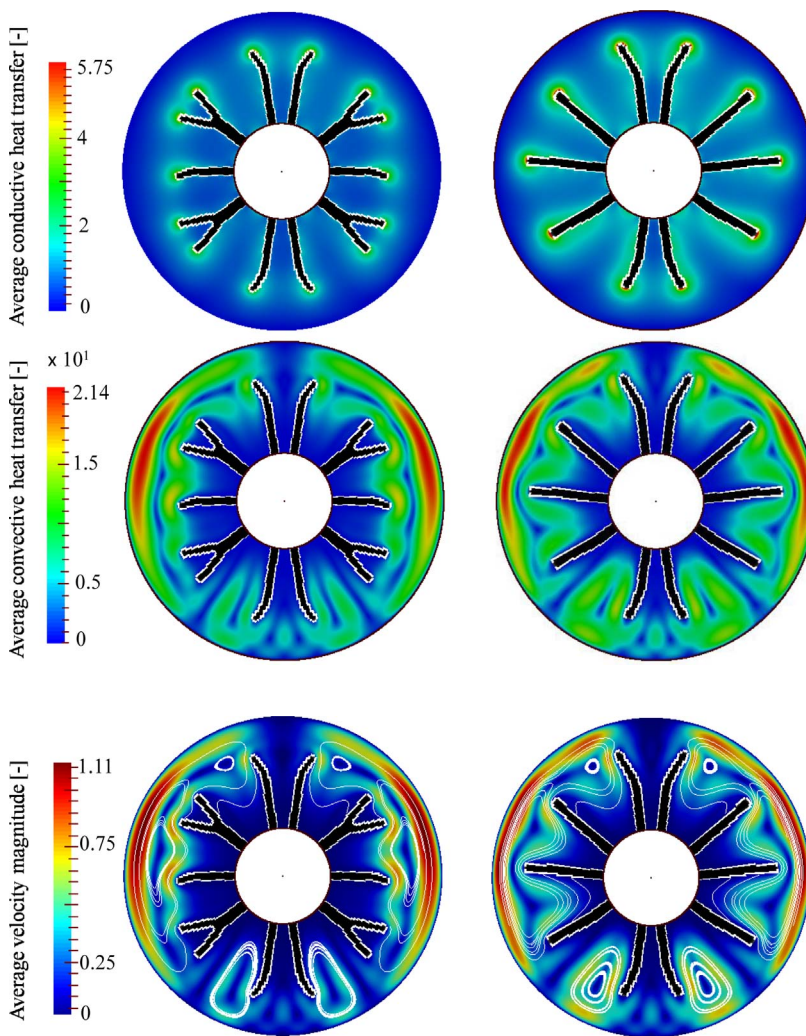


Fig. 16. Average heat conductive and convective heat transfer rate during solidification. The left column shows the diffusion design while the right column shows the solidification design.

Fig. 17. Average velocity magnitude with streamlines during solidification. The left column shows the diffusion design while the right column shows the solidification design.

the charge of the unit can be completed in 3076 s corresponding to a 37.3 % reduction of discharge time compared to the classical unit with longitudinal fins. A simplification of the geometry complexity as described in Fig. 18 results in a layout that increases the discharge time by only 256 s, corresponding to a 32.3 % improvement with respect to the longitudinal geometry. Note that the use of longitudinal fins yields a faster charge rate at the beginning of the process. The same trend was observed when comparing the melting and the diffusion design in the dimensionless case analyzed in Section 7.2. When tested during a discharge case (Fig. 20(b)), the topological design and its reduced-complexity version yield a 15.2 % and a 7.3 % reduction of discharge time

compared to the classical longitudinally finned pipe. The improvement achieved with the reduced design compared to the longitudinal layout in solidification highlights the importance of a variable length and angular distance of the fins.

The results presented in this section demonstrate the applicability of topology optimization for the practical design of fins in LHTES. The topology optimized designs as well as their modified versions for easier manufacturing yield a substantial reduction of the time required for complete charge and discharge of a storage unit for district heating applications.

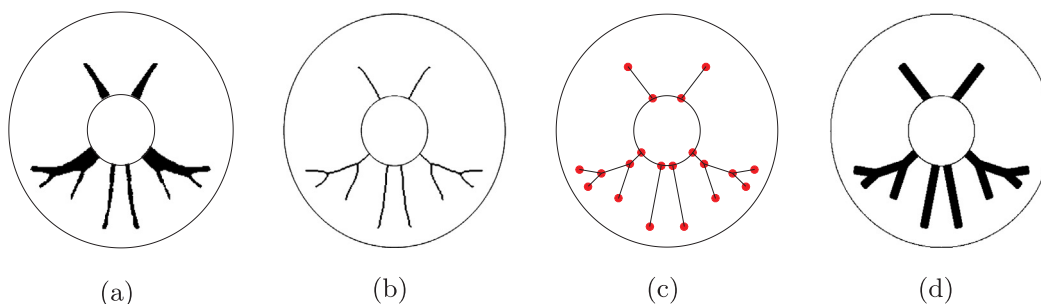


Fig. 18. Reduction of complexity of the topological melting design for easier manufacturing. (a): 300 × 300 pixelated geometry; (b): skeletonized geometry; (c): straight skeletonized geometry; (d): final geometry.

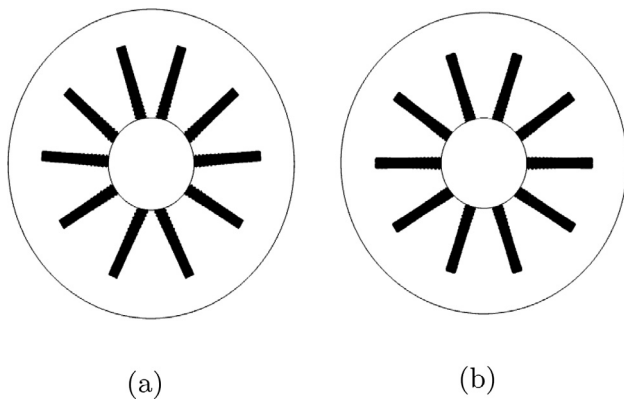


Fig. 19. (a): Reduced topological solidification geometry; (b): Reference longitudinal geometry.

8. Conclusions

In this paper, we presented a computational design optimization method for determining the layout of highly conducting fins that reduces the time needed for solidification and melting in a LHTES. The design process was formulated as a density-based topology optimization problem. Results indicate that the optimized layout obtained for

melting is fundamentally different from the one that could be obtained neglecting fluid flow. Diffusive-like fins elongate only in the bottom part of the shell leaving only a couple of short baffles at the top. This configuration results in a 27 % reduction of the time required to charge the unit up to 95 % of the total storage capacity. Geometries optimized for solidification presents minor but non-negligible modifications of some design features compared to the structure optimized for enhanced diffusion. Small details such as the absence of bifurcations and a varying branch length yield a 11 % reduction of the time required to fully discharge the unit. When tested in a small-scale storage unit for district heating applications, the topology optimized designs resulted in a 37 % and a 15 % faster charge and discharge respectively compared to a reference unit with longitudinal fins. A similar performance improvement was achieved with a modified version of the topology optimized designs, that allows for easy manufacturing and preserves the main geometrical features of the original structure.

The results obtained in this paper suggest that neglecting fluid flow in design optimization studies leads to suboptimal configurations and proved that heat transfer structures optimized for melting are in general different from those optimized for solidification. Furthermore, they present evidence that melting and solidification can be enhanced remarkably through convective transport by using finely designed fins with specific features. The identification of these features was possible thanks to the large design freedom of the presented methodology.

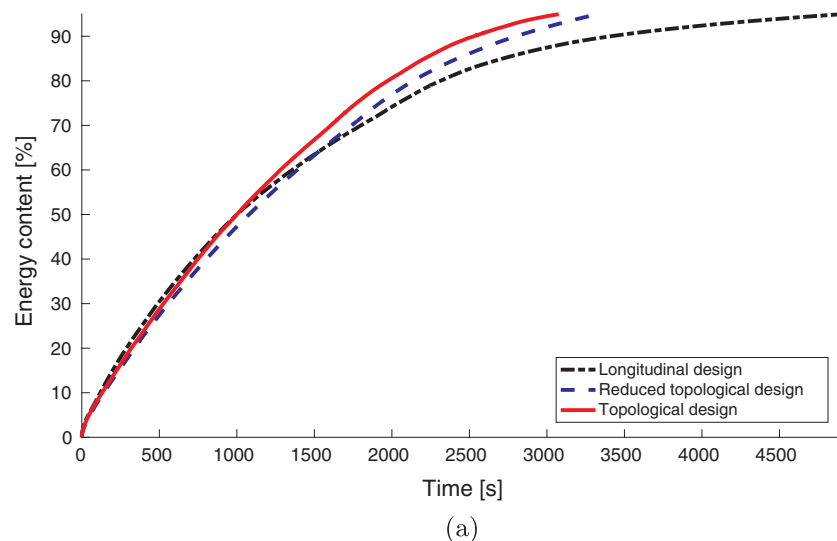
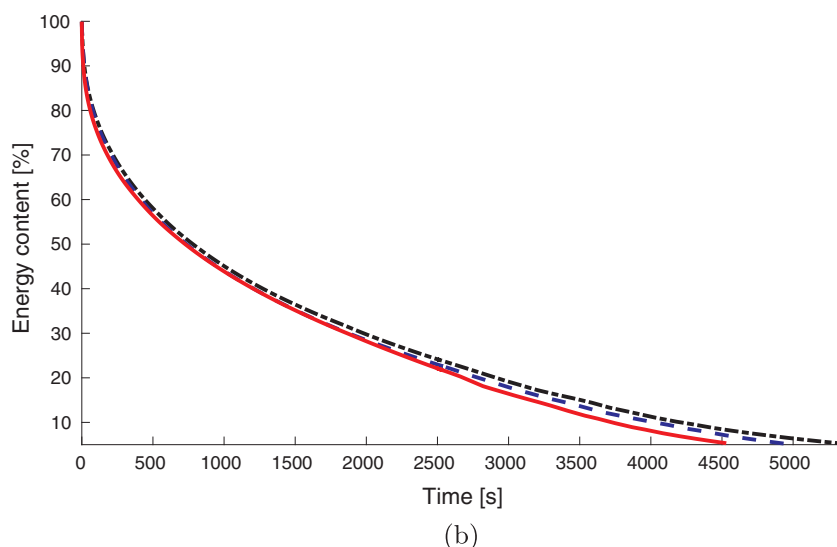


Fig. 20. Energy history during charge (a) and discharge (b).



Those would hardly be revealed by shape optimization methods considered to date for the design of LHTES. This approach has the potential to provide a definitive answer to multiple design problems in the field of LHTES and impact the technological development of these systems as demonstrated by the results of the presented case study.

This work deals only with units which undergo a complete charge or discharge. Finding layouts optimized for partial charge-discharge cycles was beyond the scope of the work but deserves attention in future research. Furthermore, future studies should investigate whether similar design trends are observable in the three-dimensional case.

Acknowledgements

The first author thanks the members of the Optimization Group at CU Boulder for their valuable advices and daily support. He gratefully acknowledges also Dr. Dell'Elce for the fruitful discussions that lead to some of the results presented in this paper.

References

- [1] Liu M, Saman W, Bruno F. Review on storage materials and thermal performance enhancement techniques for high temperature phase change thermal storage systems. *Renew Sustain Energy Rev* 2012;16(4):2118–32. <http://dx.doi.org/10.1016/j.rser.2012.01.020>.
- [2] Tatsidjodoung P, Pierrès NL, Luo L. A review of potential materials for thermal energy storage in building applications. *Renew Sustain Energy Rev* 2013;18:327–49. <http://dx.doi.org/10.1016/j.rser.2012.10.025>.
- [3] Geissbühler L, Kolman M, Zanganeh G, Haselbacher A, Steinfeld A. Analysis of industrial-scale high-temperature combined sensible/latent thermal energy storage. *Appl Therm Eng* 2016;101:657–68. <http://dx.doi.org/10.1016/j.applthermaleng.2015.12.031>.
- [4] Floros MC, Narine SS. Latent heat storage using renewable saturated diesters as phase change materials. *Energy* 2016;115:924–30. <http://dx.doi.org/10.1016/j.energy.2016.09.085>.
- [5] Colella F, Sciacovelli A, Verda V. Numerical analysis of a medium scale latent energy storage unit for district heating systems. *Energy* 2012;45(1):397–406. <http://dx.doi.org/10.1016/j.energy.2012.03.043>.
- [6] Abokersh MH, Osman M, El-Baz O, El-Morsi M, Sharaf O. Review of the phase change material (PCM) usage for solar domestic water heating systems (SDWHS). *Int J Energy Res*. <http://dx.doi.org/10.1002/er.3765>.
- [7] Agyenim F, Hewitt N, Eames P, Smyth M. A review of materials, heat transfer and phase change problem formulation for latent heat thermal energy storage systems (LHTES). *Renew Sustain Energy Rev* 2010;14(2):615–28. <http://dx.doi.org/10.1016/j.rser.2009.10.015>.
- [8] Fan L, Khodadadi J. Thermal conductivity enhancement of phase change materials for thermal energy storage: a review. *Renew Sustain Energy Rev* 2011;15(1):24–46. <http://dx.doi.org/10.1016/j.rser.2010.08.007>.
- [9] Zhang H, Baeyens J, Caceres G, Degreve J, Lv Y. Thermal energy storage: recent developments and practical aspects. *Prog Energy Combust Sci* 2016;53:1–40. <http://dx.doi.org/10.1016/j.pecs.2015.10.003>.
- [10] Li G, Zheng X. Thermal energy storage system integration forms for a sustainable future. *Renew Sustain Energy Rev* 2016;62:736–57. <http://dx.doi.org/10.1016/j.rser.2016.04.076>.
- [11] Ibrahim NI, Al-Sulaiman FA, Rahman S, Yilbas BS, Sahin AZ. Heat transfer enhancement of phase change materials for thermal energy storage applications: a critical review. *Renew Sustain Energy Rev* 2017;74:26–50. <http://dx.doi.org/10.1016/j.rser.2017.01.169>.
- [12] Chiu JN, Martin V. Submerged finned heat exchanger latent heat storage design and its experimental verification. *Appl Energy* 2012;93:507–16. <http://dx.doi.org/10.1016/j.apenergy.2011.12.019>.
- [13] Tay N, Belusko M, Castell A, Cabeza L, Bruno F. An effectiveness-NTU technique for characterising a finned tubes PCM system using a CFD model. *Appl Energy* 2014;131:377–85. <http://dx.doi.org/10.1016/j.apenergy.2014.06.041>.
- [14] Mat S, Al-Abidi AA, Sopian K, Sulaiman M, Mohammad AT. Enhance heat transfer for PCM melting in triplex tube with internal-external fins. *Energy Convers Manage* 2013;74:223–36. <http://dx.doi.org/10.1016/j.enconman.2013.05.003>.
- [15] Tay N, Bruno F, Belusko M. Experimental validation of a CFD model for tubes in a phase change thermal energy storage system. *Int J Heat Mass Transf* 2012;55(4):574–85. <http://dx.doi.org/10.1016/j.ijheatmasstransfer.2011.10.054>.
- [16] Kozak Y, Rozenfeld T, Ziskind G. Close-contact melting in vertical annular enclosures with a non-isothermal base: theoretical modeling and application to thermal storage. *Int J Heat Mass Transf* 2014;72:114–27. <http://dx.doi.org/10.1016/j.ijheatmasstransfer.2013.12.058>.
- [17] Mao Q. Recent developments in geometrical configurations of thermal energy storage for concentrating solar power plant. *Renew Sustain Energy Rev* 2016;59:320–7. <http://dx.doi.org/10.1016/j.rser.2015.12.355>.
- [18] Jegadheeswaran S, Pohekar SD. Performance enhancement in latent heat thermal storage system: a review. *Renew Sustain Energy Rev* 2009;13(9):2225–44. <http://dx.doi.org/10.1016/j.rser.2009.06.024>.
- [19] Pizzolato A, Sharma A, Maute K, Sciacovelli A, Verda V. Topology optimization for heat transfer enhancement in latent heat thermal energy storage. *Int J Heat Mass Transf* 2017;113:875–88. <http://dx.doi.org/10.1016/j.ijheatmasstransfer.2017.05.098>.
- [20] Sciacovelli A, Gagliardi F, Verda V. Maximization of performance of a PCM latent heat storage system with innovative fins. *Appl Energy* 2015;137:707–15. <http://dx.doi.org/10.1016/j.apenergy.2014.07.015>.
- [21] Vogel J, Felbinger J, Johnson M. Natural convection in high temperature flat plate latent heat thermal energy storage systems. *Appl Energy* 2016;184:184–96. <http://dx.doi.org/10.1016/j.apenergy.2016.10.001>.
- [22] Darzi AAR, Jourabian M, Farhadi M. Melting and solidification of PCM enhanced by radial conductive fins and nanoparticles in cylindrical annulus. *Energy Convers Manage* 2016;118:253–63. <http://dx.doi.org/10.1016/j.enconman.2016.04.016>.
- [23] Beck A, Koller M, Walter H, Hameter M. Transient numerical analysis of different finned tube designs for use in latent heat thermal energy storage devices. In: Proceedings of the ASME 2015 9th international conference on energy sustainability, ASME international; 2015. <http://dx.doi.org/10.1115/es2015-49145>.
- [24] Wang F, Maidment G, Missenden J, Tozer R. The novel use of phase change materials in refrigeration plant. Part 3: PCM for control and energy savings. *Appl Therm Eng* 2007;27(17–18):2911–8. <http://dx.doi.org/10.1016/j.applthermaleng.2005.06.010>.
- [25] Tay N, Bruno F, Belusko M. Experimental investigation of dynamic melting in a tube-in-tank PCM system. *Appl Energy* 2013;104:137–48. <http://dx.doi.org/10.1016/j.apenergy.2012.11.035>.
- [26] Bendsoe MP. Optimal shape design as a material distribution problem. *Struct Optim* 1989;1(4):193–202. <http://dx.doi.org/10.1007/bf01650949>.
- [27] Zhou M, Rozvany G. The COC algorithm, part II: topological, geometrical and generalized shape optimization. *Comput Methods Appl Mech Eng* 1991;89(1–3):309–36. [http://dx.doi.org/10.1016/0045-7825\(91\)90046-9](http://dx.doi.org/10.1016/0045-7825(91)90046-9).
- [28] Deaton JD, Grandhi RV. A survey of structural and multidisciplinary continuum topology optimization: post 2000. *Struct Multidiscip Optim* 2013;49(1):1–38. <http://dx.doi.org/10.1007/s00158-013-0956-z>.
- [29] Gersborg-Hansen A, Sigmund O, Haber R. Topology optimization of channel flow problems. *Struct Multidiscip Optim* 2005;30(3):181–92. <http://dx.doi.org/10.1007/s00158-004-0508-7>.
- [30] Kreissl S, Pingen G, Maute K. Topology optimization for unsteady flow. *Int J Numer Methods Eng* 2011;n/a–. <http://dx.doi.org/10.1002/nme.3151>.
- [31] Nørgaard S, Sigmund O, Lazarov B. Topology optimization of unsteady flow problems using the lattice Boltzmann method. *J Comput Phys* 2016;307:291–307. <http://dx.doi.org/10.1016/j.jcp.2015.12.023>.
- [32] Makhija D, Maute K. Level set topology optimization of scalar transport problems. *Struct Multidiscip Optim* 2014;51(2):267–85. <http://dx.doi.org/10.1007/s00158-014-1142-7>.
- [33] Yoon GH. Topological design of heat dissipating structure with forced convective heat transfer. *J Mech Sci Technol* 2010;24(6):1225–33. <http://dx.doi.org/10.1007/s12206-010-0328-1>.
- [34] Alexandersen J, Aage N, Andreassen CS, Sigmund O. Topology optimisation for natural convection problems. *Int J Numer Methods Fluids* 2014;76(10):699–721. <http://dx.doi.org/10.1002/flid.3954>.
- [35] Coffin P, Maute K. A level-set method for steady-state and transient natural convection problems. *Struct Multidiscip Optim* 2015;53(5):1047–67. <http://dx.doi.org/10.1007/s00158-015-1377-y>.
- [36] Sopranì S, Haertel J, Lazarov B, Sigmund O, Engelbrecht K. A design approach for integrating thermoelectric devices using topology optimization. *Appl Energy*, vol. 176, p. 49–64. <http://dx.doi.org/10.1016/j.apenergy.2016.05.024>.
- [37] Sciacovelli A, Colella F, Verda V. Melting of PCM in a thermal energy storage unit: numerical investigation and effect of nanoparticle enhancement. *Int J Energy Res* 2012;37(13):1610–23. <http://dx.doi.org/10.1002/er.2974>.
- [38] Shmueli H, Ziskind G, Letan R. Melting in a vertical cylindrical tube: numerical investigation and comparison with experiments. *Int J Heat Mass Transf* 2010;53(19–20):4082–91. <http://dx.doi.org/10.1016/j.ijheatmasstransfer.2010.05.028>.
- [39] Borrvall T, Petersson J. Topology optimization of fluids in Stokes flow. *Int J Numer Methods Fluids* 2003;41(1):77–107. <http://dx.doi.org/10.1002/flid.426>.
- [40] Voller VR, Swaminathan CR, Thomas BG. Fixed grid techniques for phase change problems: a review. *Int J Numer Methods Eng* 1990;30(4):875–98. <http://dx.doi.org/10.1002/nme.1620300419>.
- [41] Hughes TJ, Franca LP, Balestra M. A new finite element formulation for computational fluid dynamics: V. circumventing the babuška-brezzi condition: a stable Petrov-Galerkin formulation of the stokes problem accommodating equal-order interpolations. *Comput Methods Appl Mech Eng* 1987;62(1):111. [http://dx.doi.org/10.1016/0045-7825\(87\)90093-4](http://dx.doi.org/10.1016/0045-7825(87)90093-4).
- [42] Brooks AN, Hughes TJ. Streamline upwind/Petrov-Galerkin formulations for convection dominated flows with particular emphasis on the incompressible Navier-Stokes equations. *Comput Methods Appl Mech Eng* 1982;32(1–3):199–259. [http://dx.doi.org/10.1016/0045-7825\(82\)90071-8](http://dx.doi.org/10.1016/0045-7825(82)90071-8).
- [43] Ilinca F, Héty J-F. Galerkin gradient least-squares formulations for transient conduction heat transfer. *Comput Methods Appl Mech Eng* 2002;191(27–28):3073–97. [http://dx.doi.org/10.1016/s0045-7825\(02\)00242-6](http://dx.doi.org/10.1016/s0045-7825(02)00242-6).
- [44] Kreissl S, Pingen G, Maute K. Topology optimization for unsteady flow. *Int J Numer Methods Eng* 2011;n/a–. <http://dx.doi.org/10.1002/nme.3151>.
- [45] Gartling DK, Hogan RE, Glass MW. COYOTE: a finite element computer program for nonlinear heat conduction problems. Part I, theoretical background. Tech rep; Mar 2010. <http://dx.doi.org/10.2172/986602>.
- [46] Giles MB, Pierce NA. An introduction to the adjoint approach to design. *Flow, Turbul Combust* 2000;65(3–4):393–415.
- [47] Coffin P, Maute K. A level-set method for steady-state and transient natural

- convection problems. *Struct Multidiscip Optim* 2015;53(5):1047–67. <http://dx.doi.org/10.1007/s00158-015-1377-y>.
- [48] Sigmund O, Petersson J. Numerical instabilities in topology optimization: a survey on procedures dealing with checkerboards, mesh-dependencies and local minima. *Struct Optim* 1998;16(1):68–75. <http://dx.doi.org/10.1007/bf01214002>.
- [49] Bruns TE, Tortorelli DA. Topology optimization of non-linear elastic structures and compliant mechanisms. *Comput Methods Appl Mech Eng* 2001;190(26–27):3443–59. [http://dx.doi.org/10.1016/s0045-7825\(00\)00278-4](http://dx.doi.org/10.1016/s0045-7825(00)00278-4).
- [50] Wang F, Lazarov BS, Sigmund O. On projection methods, convergence and robust formulations in topology optimization. *Struct Multidiscip Optim* 2010;43(6):767–84. <http://dx.doi.org/10.1007/s00158-010-0602-y>.
- [51] Sigmund O, Maute K. Topology optimization approaches. *Struct Multidiscip Optim* 2013;48(6):1031–55. <http://dx.doi.org/10.1007/s00158-013-0978-6>.
- [52] Alexandersen J, Sigmund O, Aage N. Large scale three-dimensional topology optimization of heat sinks cooled by natural convection. *Int J Heat Mass Transf* 2016;100:876–91.
- [53] Amestoy PR, Duff IS, L'Excellent J-Y. Multifrontal parallel distributed symmetric and unsymmetric solvers. *Comput Methods Appl Mech Eng* 2000;184(2):501–20. [http://dx.doi.org/10.1016/s0045-7825\(99\)00242-x](http://dx.doi.org/10.1016/s0045-7825(99)00242-x).
- [54] Svanberg K. A globally convergent version of mma without linesearch, in: *Proceedings of the first world congress of structural and multidisciplinary optimization*, vol. 28, Goslar, Germany; 1995. p. 9–16.
- [55] Gau C, Viskanta R. Melting and solidification of a pure metal on a vertical wall. *J Heat Transf* 1986;108(1):174. <http://dx.doi.org/10.1115/1.3246884>.
- [56] Pal D, Joshi YK. Melting in a side heated tall enclosure by a uniformly dissipating heat source. *Int J Heat Mass Transf* 2001;44(2):375–87. [http://dx.doi.org/10.1016/s0017-9310\(00\)00116-2](http://dx.doi.org/10.1016/s0017-9310(00)00116-2).
- [57] COMSOL, version 5.0, COMSOL Inc., Burlington, MA, USA; 2014.
- [58] Sigmund O. Morphology-based black and white filters for topology optimization. *Struct Multidiscip Optim* 2007;33(4–5):401–24. <http://dx.doi.org/10.1007/s00158-006-0087-x>.
- [59] Agyenim F, Eames P, Smyth M. A comparison of heat transfer enhancement in a medium temperature thermal energy storage heat exchanger using fins. *Sol Energy* 2009;83(9):1509–20. <http://dx.doi.org/10.1016/j.solener.2009.04.007>.
- [60] Al-Abidi AA, Mat S, Sopian K, Sulaiman M, Mohammad AT. Experimental study of melting and solidification of PCM in a triplex tube heat exchanger with fins. *Energy Build* 2014;68:33–41. <http://dx.doi.org/10.1016/j.enbuild.2013.09.007>.
- [61] Rathod MK, Banerjee J. Thermal performance enhancement of shell and tube latent heat storage unit using longitudinal fins. *Appl Therm Eng* 2015;75:1084–92. <http://dx.doi.org/10.1016/j.applthermaleng.2014.10.074>.
- [62] Laing D, Bauer T, Breidenbach N, Hachmann B, Johnson M. Development of high temperature phase-change-material storages. *Appl Energy* 2013;109:497–504. <http://dx.doi.org/10.1016/j.apenergy.2012.11.063>.
- [63] Olcese M. Echangeur thermique pour systeme de stockage thermique, wO Patent App. PCT/EP2013/070,849; Apr. 17 2014.
- [64] Wang P, Yao H, Lan Z, Peng Z, Huang Y, Ding Y. Numerical investigation of PCM melting process in sleeve tube with internal fins. *Energy Convers Manage* 2016;110:428–35. <http://dx.doi.org/10.1016/j.enconman.2015.12.042>.
- [65] Sciacovelli A, Verda V. Second-law design of a latent heat thermal energy storage with branched fins. *Int J Numer Methods Heat Fluid Flow* 2016;26(2):489–503. <http://dx.doi.org/10.1108/hff-01-2015-0040>.
- [66] Zegard T, Paulino GH. Bridging topology optimization and additive manufacturing. *Struct Multidiscip Optim* 2015;53(1):175–92. <http://dx.doi.org/10.1007/s00158-015-1274-4>.
- [67] Cuillière J-C, François V, Nana A. Automatic construction of structural CAD models from 3d topology optimization. *Comput-Aided Des Appl* 2017;1–15. <http://dx.doi.org/10.1080/16864360.2017.1353726>.
- [68] Pratt WK. Digital image processing. John Wiley & Sons, Inc.; 2007.